University of Bath

Alternative formats
If you require this document in an alternative format, please contact:
openaccess@bath.ac.uk

Low burden, adsorbent and heat absorbing structures for respiratory protection in building fires

Jonathan E. Barnard[a], Stuart Scott[a], Steve Tennison[b], Martin W. Smith[c], Andrew D. Burrows[a,d], Semali Perera[a,e], Y. M. John Chew[a,e]*

[a] *Centre for Sustainable & Circular Technologies, University of Bath, Bath, BA2 7AY, UK.*

[b] *Carbon Tex Ltd., 62 Farleigh Road, Addlestone, Surrey, KT15 3HR.*

[c] *CBR Division, Defence Science & Technology Laboratory, Porton Down, Salisbury, SP4 0JQ, UK.*

[d] *Department of Chemistry, University of Bath, University of Bath, Bath, BA2 7AY, UK.*

[e] *Centre for Advanced Separations Engineering, Department of Chemical Engineering, University of Bath, Bath, BA2 7AY, UK.*

*Corresponding author (jc604@bath.ac.uk)

Abstract

The primary function of commercial fire escape masks (FEMs), fitted with granulated activated carbon (AC) packed bed filters, is to provide at least 15 minutes of respiratory protection by removing toxic gases and particulates from surrounding air in building fires. In this work, the extended functionality of heat entrapment and its impact on inhalation temperature by using shape-stable phase change material whilst maintaining low pressure drop is reported for the first time. The proposed filter contained an array of monoliths where each monolith consisted of three functional sections, namely the pre-cooler, AC adsorbent section and post-cooler. The pre- and post- coolers consisted of polyethylene glycol 4000/triallyl isocyanurate and were intended to absorb environmental and process heats from the inhaled atmosphere. Numerical models were developed to describe the species and energy transport within the monolith filters and were

1

compared against packed bed filters. The representative challenge conditions were set at an inhalation rate of 50 L min^{-1}, trace amount of butane (1000 ppm) and inlet air temperature of 80 °C. The best performing filter contained nine monoliths each with density of 734 channels per square inch, and could protect the user from excessive inhalation temperatures for 22 min and butane breakthrough for approximately 14 min whilst maintaining low pressure drop of 27.4 Pa. In comparison to an equivalent mass packed bed, the monolith provided additional high temperature protection, extended butane breakthrough time by a maximum of 84% and reduced pressure drop by 25%. This work demonstrates promising opportunities to move the FEM industry forward and the possibility for the technology to be used in general industrial respirators in applications such as agriculture, chemical and pharmaceutical industries.

1. Introduction

Residential fires accounted for above 70% of all fire fatalities in the UK between 2010-2019 [1] and 83% of fatalities in the US between 2013-2015 [2]. However, protection of residents from the inhalation of toxic gases at elevated temperatures in the event of dwelling fires using emergency fire escape masks (FEMs) remains an uncommon practice. A leading cause of death was smoke inhalation and eventual asphyxiation due to toxic gases [2,3]. Burns to the respiratory system have been recognised as a significant risk factor in relation to increased mortality rates, hospital stay and number of surgeries when compared to patients without respiratory burns [4,5]. Inhalation

2

burns present a secondary protection challenge and would require the FEM to absorb environmental heat generated by the fire and heat generated within the device's filter by the exothermic process of gas adsorption and reaction. A summary of the challenges posed by building fires is described in Figure 1.

Figure 1: Infographic describing the current challenges posed by building fires, the capability of current standard commercial FEMs and the proposed future changes to improve upon existing filter devices [2,6–15].

To provide respiratory and sensory protection from building fires, FEMs must create a barrier to multiple hazards. Firstly, numerous hazardous gaseous components must be captured by the FEM. The four gaseous species that cause death via asphyxiation in fires are carbon monoxide (CO), hydrogen cyanide (HCN), carbon dioxide (CO_2) and low oxygen (O_2) [16]. Ultimately these gases result in unconsciousness and death due to tissue hypoxia. CO_2 also causes hyperventilation

which increases the rate of uptake of both asphyxiant and irritant gases, further reducing the chances of escape [17]. Secondly, although irritants are not the main cause of death in fires, they often reduce the chance of escape by causing sensory irritation [18]. These include smoke particles, sulfur oxides (SO_x), nitrogen oxides (NO_x), acid gases such as hydrogen chloride (HCl) and volatile organic compounds (VOCs) including formaldehyde and acrolein [19]. Thirdly, in addition to harmful gases, the high temperatures and heat generated by fires cause surface burns to the skin and respiratory tract. Modelling studies have suggested tissue damage occurs if the person breathes in dry air above 85 °C [11] and in humid environments, tracheal burns can occur above 60 °C [12], much lower than air temperatures commonly found in areas of a building away from the origin of the fire, where temperatures can increase above 80 °C [20–22]. Finally, the FEM must have a low breathing burden, weight, be reasonably cheap and compact. The British European standard (BS EN 403:2004) for 'Respiratory protective devices for self-rescue' specifies an upper limit of 800 Pa for breathing resistance, 1 kg for total device weight (including the protective hood) and a minimum use time of 15 minutes before breakthrough of toxic gases [13].

Commercially available emergency escape masks often consist of a hood with tight-fitting filter and neck seals, providing a complete barrier to the external environment. Placed within the hood is an internal half mask to which the respiratory canister attaches [7,15]. The user inhales through the canister whereupon the toxic air is purified. Exhalation is managed via separate exhalation valves. Within the canisters there are multiple layers of functional materials which can include a variety of particulate filters, adsorbent solids and catalysts [23]. Particulate filters are required to remove larger particulates such as dust, aerosols or soot and are typically made from fine fibrous materials, such as plastic, glass or paper fibers, randomly woven to increase contact

4

between the particulate and filter material [24]. The adsorbent solid and catalyst are often included within the canister as a granular packing and can either be arranged as separate layers or the adsorbent can be chemically impregnated with catalysts. Activated carbons (ACs) have been favoured as the adsorbent solid historically due to their high BET surface areas (typically between 400-1200 m^2 g^{-1}), ability to adsorb a range of pollutants and toxins within humid environments due to their inherent hydrophobicity and their inert nature with respect to metal impregnates, allowing modification of the carbon surface and the inclusion of chemisorption properties [25–27]. Furthermore, ACs are easy to obtain and prepare from a range of sources with good mechanical properties [25]. A widely used reactive metal catalyst in FEMs used for the purpose of low temperature oxidation of CO into CO_2 is Hopcalite. Low temperature oxidation of CO has been comprehensively studied and alternative catalysts with promising results include cobalt oxide (Co_3O_4) nanorods [28] and gold nanoparticles on base transition metal oxides [29].

Although commercial escape masks have gained widespread use in industrial and medical settings, with the Occupational Safety and Health Administration (OSHA) estimating 5.0 million workers wear respirators in their workplace [30], the use of escape masks in domestic dwellings and high-rise buildings remains uncommon. This has been attributed to a wide range of factors including a lack of awareness of the dangers posed by toxic gases, a lack of legislation surrounding use by emergency services and civilians, the affordability, weight and discomfort of the device, psychological barriers in adopting the device and breathing difficulties due to the filters [14,31]. These barriers to widespread adoption highlight the need for filters which no longer rely on packed bed designs which force the inhaled air on a tortuous path increasing the pressure drop across the filter.

Monoliths are continuous unitary structures with numerous parallel passages cutting through the length of the structure [32]. The channels are separated by thin walls in the region of 0.5 - 4.0 mm thick allowing for a cell density between 300 - 1200 cells per square inch (CPI) [33]. Monoliths incur low pressure drop compared to packed beds due to the straight channels in addition to minimal diffusion distances, permitting effective toxic component mass transfer into the monolith walls [34]. For the purposes of gas purification AC monoliths have been produced by extrusion of a partially cured phenolic resin through a die to give the desired channel shape. The extruded phenolic resin is fused to form a continuous solid, carbonised to remove volatiles and produce a char and finally activated to create micropores [27,35,36]. AC monoliths based on this production method have been successfully applied to purification of gas streams containing CO_2 [37,38] and volatile organic compounds (VOCs) such as methane [38], dichloromethane (DCM) [39] and butane [40] and show similar capacity and mass transfer performance when compared to an equivalent mass packed bed. Due to the low pressure drop, comparable kinetic performance to packed bed and ease of production, AC monoliths were chosen in this work as a viable candidate for incorporation into the proposed face mask filter.

Herein we investigate the feasibility of using monolithic filters within FEMs by using numerical methods to simulate the species and energy transport within the device. The performance of a prototype monolith filter was compared to that of a typical commercial packed bed filter using the identified areas of improvement which included (i) reduction of the inhalation burden, (ii) improvement of the capacity and kinetic performance to physically adsorb harmful gases and (iii) the extended capability to remove environmental and process heats whilst maintaining a low weight and cost effective device. The basis of comparison was based on

6

numerical models which investigated the mass, momentum and energy balances for both types of filter using ANSYS CFX 17.0 computational fluid dynamics software. Single component adsorption was studied with 1000 ppm butane within an inert atmosphere as the challenge gas, entering at 80 ºC, to mimic a high temperature toxic gas moving through the filter. Butane is commonly used as a test gas to provide an analogue to VOCs [41], such as acrolein or formaldehyde, which would be present in the atmosphere during a fire. Trace butane adsorption isotherms were obtained from literature to provide valid adsorbate uptake values. The SS-PCM selected for investigation in this study was polyethylene glycol (PEG) 4000 / triallyl isocyanurate (PEG/TAIC). Differential scanning calorimetry (DSC) curves were generated for this composite to verify the latent heat and phase change temperature of our samples. To the best of the authors' knowledge there is currently no commercial emergency respirator that includes coupled gas adsorption and heat removal capabilities. Therefore, this research presents a significant area for improvement and opens up opportunity to move the respiratory protection equipment industry forward with new low burden filters in a wide range of applications, including for escape applications for emergency responders and the general public.

2. Fire Escape Mask Prototype

The prototype FEM filter incorporated both an AC adsorbent component to purify the inhaled toxic gas stream and heat absorbing component to remove environmental and process heats. One possible configuration of the proposed filter is depicted in Figure 2. Figure 2 (a) shows that the initial prototype FEMs is comprised of two filters fitted to a half mask, which would then be fitted within a hood (not shown), as is common with commercial FEMs. Figure 2 (b) shows an axial cross section of an individual monolith and a section of an individual monolith channel,

highlighting the dimensions of the channel and channel wall. Figure 2 (c) displays the prototype in an expanded view and provides further information regarding the potential device dimensions and highlights that each cartridge will contain nine squared face monoliths arranged in a square array to maximise space efficiency. Each monolith has an equal height and width of 22.5 mm and a length, L, of 50.0 mm. Each monolith consists of three functional components, two heat absorbing components each of 12.5 mm in length which were defined as the pre- and post-cooler sections made from a shape-stable phase change material (SS-PCM) and a 25.0 mm central phenolic resin derived AC section to adsorb toxic gases. Both the SS-PCM and AC were assumed to have been extruded with identical cross sectional profiles. A particulate filter preceded the monoliths to remove larger particulates.
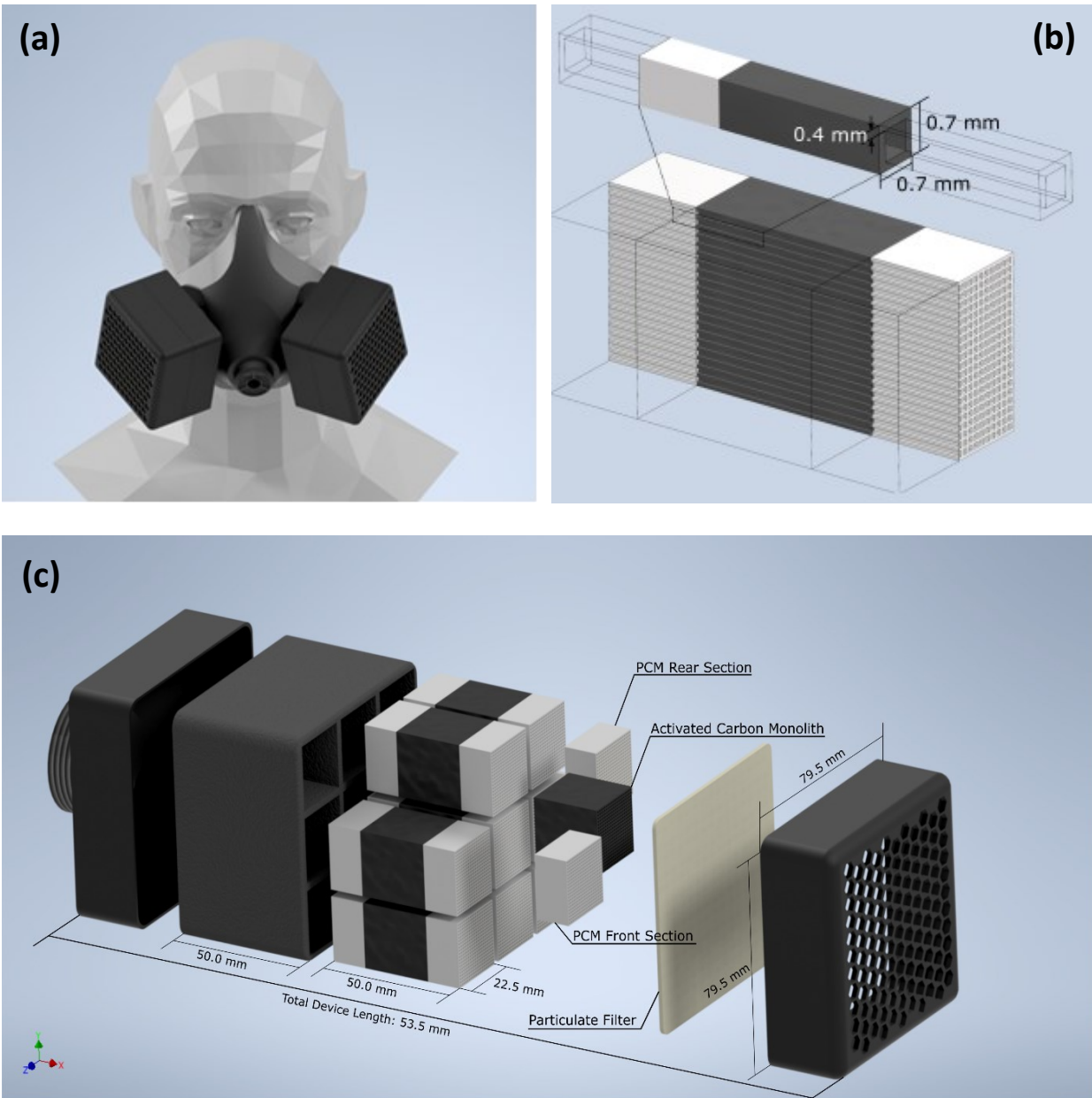
*Figure 2: Overall configuration of the proposed monolithic FEM displaying the **(a)** inner half mask and filters (hood excluded) , **(b)** individual monolith and channel and **(c)** expanded view of individual components of the filter.*

3. Heat Absorption

SS-PCMs are commonly used in thermal energy storage and management due to their high storage

capacity. Applications include renewable energy storage, temperature regulation in buildings, heat

exchangers and within textiles, including personal protective equipment (PPE) to prevent the overheating of workers [42–44]. The advantage of using SS-PCMs arises from the utilisation of the latent heat capacity during phase change, permitting greater amounts of heat absorption than sensible heat alone.

SS-PCMs were considered as potential candidates to remove the environmental and heats generated from adsorption and/or reactions. SS-PCMs generally consist of a material that changes phase within the operating temperature range of a given process and a shape stabilising matrix which entraps the often long molecular chain PCM within its structure [45]. The shape stabilising matrix offers an inherently safer design by preventing the PCM leaching and stopping volume change upon the PCM changing phase in the monolith filter. Due to the selected operating temperature range of 25-80 °C in this study, focus was placed on solid-liquid PCMs which offer numerous materials changing phase within the specified range. Solid-liquid PCMs can be categorised into organic and inorganic. Organic PCMs include paraffins, fatty acids and polymers which offer reasonable latent heat capacity, are inert, non-corrosive, non-toxic but can be expensive and have low density and thermal conductivity. Inorganic PCMs, such as salt hydrates and eutectic salts, have greater latent heats and thermal conductivities but incur volume change, leakage and are corrosive and often breakdown upon multiple heating cycles [43,46,47]. Aside from having excellent thermal characteristics the SS-PCM chosen must also have favorable physical, chemical and economic features as displayed in Table 1.

The SS-PCM selected for investigation in this study was of polyethylene glycol (PEG) 4000 / triallyl isocyanurate (PEG/TAIC) with a 9:1 PCM:SS ratio which had a latent heat capacity of 135.7 J g^{-1} and a phase change temperature of 57.1 °C [48]. Huang *et al.* [48], also reported

insignificant changes in thermal properties after 200 thermal cycles above and below the phase change temperature, no liquid leakage and complete shape stabilisation (no visible phase change). A full review of potential SS-PCM candidates has been outlined in Table S1 of the Supporting Information.

Table 1: Desirable features of SS-PCM for the application of an emergency respiratory filter [45,49,50].

Properties	Desirable features
Thermal	• Phase change temperature between 40-60°C. Preventing premature or high temperature phase change. • High latent heat capacity, providing extended isothermal operation. • High specific heat capacity, providing additional sensible heat storage. • High thermal conductivity, allowing rapid transfer of heat from gas to the SS-PCM.
Physical	• High bulk density to maximise specific & latent heats. • No density changes during phase change to prevent damage to the filter. • Processable/moldable to enable integration into the device.
Chemical	• Non-flammable. • Non-toxic. • Non-corrosive to surrounding materials.
Economic / Sustainable	• Abundant. • Cost effective. • Ease of disposal.

4. Numerical models

Two systems were considered, the proposed monolithic configuration (Figure 2) and a packed bed filter consisting solely of a granular AC (GAC) to represent a commercially available filter. The monolith configuration was compared against the packed bed filter, as a benchmark, in terms of pressure drop, adsorption performance and the impact of including of a heat absorbing SS-PCM component. In both systems, the transport and adsorption phenomena were modelled in three dimensions. The conditions used to compare both devices are summarised in Table 2.

Table 2: Operating conditions for the monolithic and packed bed FEMs.

Total mask flow rate [L min^{-1}]	Individual monolith flow rate [L min^{-1}]	Individual packed bed flow rate [L min^{-1}]	Inlet butane fraction [ppm]	Inlet gas temperature [ºC]	Initial device temperature [ºC]
50	2.8	25	1000	80	25

4.1 Model geometries

To model a commercial packed bed filter, 1/32 of a single packed bed cartridge with diameter, d_{pb}, was considered, as shown in Figure 3 (a). The geometry consisted of a small inlet and outlet section, each with length, L_e, before the channel inlet to mimic an ambient atmosphere and the outlet conditions within the FEM hood directly before the gas is inhaled by the user, respectively. A packed bed domain consisting of spherical adsorbent carbon packing, with a particle diameter, d_p, of 1 mm, to adsorb the harmful components within the gas stream was defined as length, L_a.

For the monolith filter 1/8 of a single channel was modelled, as shown in Figure 3 (b). This geometry also consisted of a small inlet and outlet sections of length, L_e. The filter was comprised of three functional domains including two heat absorbing sections consisting of SS-PCM with length, L_{pcm}, which were situated before and after the adsorbent section, labelled as the pre- and post-cooler sections, respectively. All dimensions are summarised in Table 3.

The primary role of the pre-cooler is to mitigate the environmental heat generated by the fire to reduce the inhalation temperature and to reduce the temperature of the gas within the porous adsorbent to increase the maximum equilibrium adsorbate uptake. The role of the post-cooler is to

extend the protection against environmental heat whilst removing heat generated by adsorption or reaction. The phenolic resin derived adsorbent AC section with length, L_a, was placed at the centre of the structure to remove toxic gaseous components.
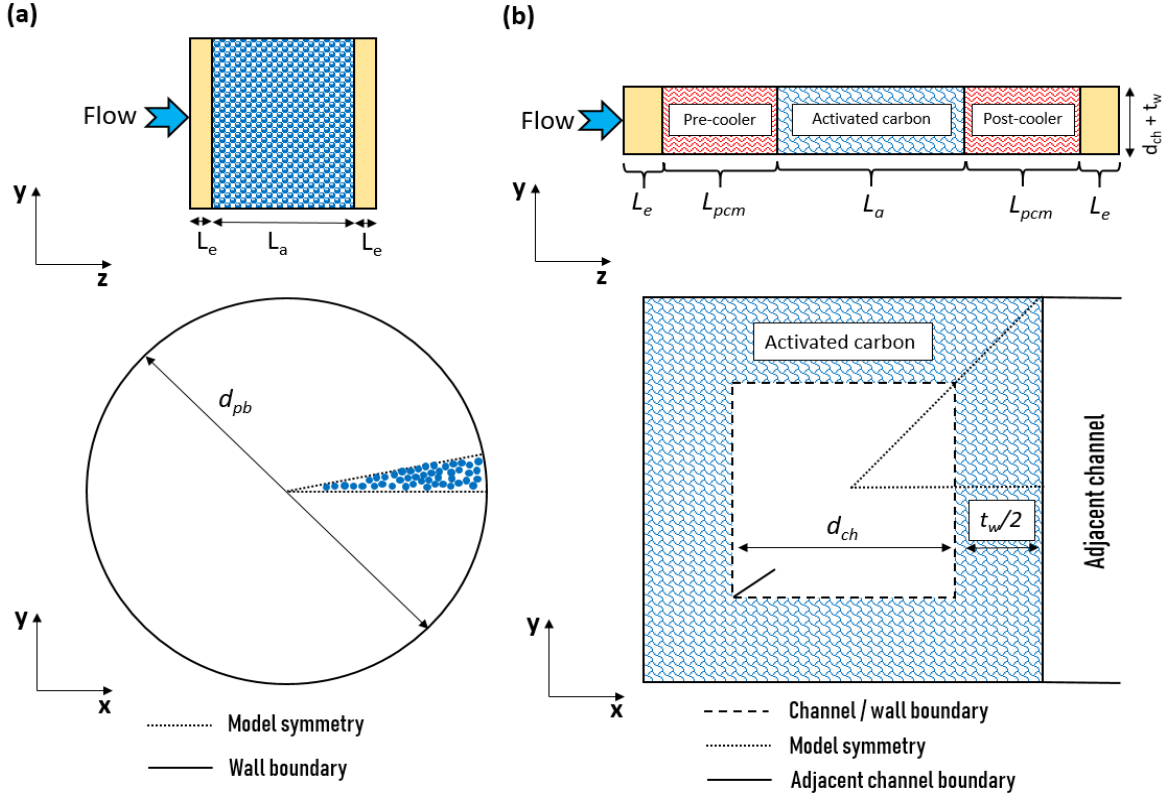

Figure 3: (a) Packed bed and (b) square channel monolith highlighting the domains and boundaries incorporated into the numerical model. All dimensions are summarised in Table 3.

Table 3: Summary of the dimensions and bulk voidage used in the numerical model and the adsorbent mass within a single SRD cartridge.

| CPI | Square channel monoliths | | | | | | Packed bed | | | | Similar properties |
	d_{ch} [mm]	t_w [mm]	ε_b [-]	L_a [cm]	L_{pcm} [cm]	L_e [cm]	d_{pb} [cm]	ε_b [-]	L_a [cm]	L_e [cm]	m_a [g]
509	0.7	0.4	0.39	2.5	1.25	0.075	7.7	0.4	2.5	0.25	54
734	0.5	0.4	0.28	2.5	1.25	0.075	7.7	0.4	2.9	0.25	63
1225	0.3	0.4	0.17	2.5	1.25	0.075	7.7	0.4	3.4	0.25	73

In addition to utilising symmetry to reduce computational resources required, extensive mesh and time-step studies were completed to ensure efficient, stable and accurate solutions. Full details of these studies can be found in the Supporting Information Section S2.3.

To optimise the monolith configuration the channel width, d_{ch}, was varied whilst the wall thickness, t_w, was maintained constant to determine the impact of varying the CPI on the butane and temperature breakthrough characteristics. A constant t_w of 0.4 mm was chosen in this study to maintain consistency with the monoliths generated in our laboratories. Previous studies [51] have shown that a t_w of 0.44 mm should not be exceeded to maintain a comparable linear driving force (LDF) coefficient, k_a, and therefore a similar internal adsorptive mass transfer to a packed bed system. The monolith and packed bed systems were compared on an equal adsorbent mass, m_a, basis. For each monolith with a differing CPI an equivalent mass packed bed system was created by varying length of the packed bed. This assumed a similar particle density, ρ_p, for the adsorbent of 774 kg m^{-3} and an average bulk voidage, ε_b, of 0.4 for the packed bed. The key geometric dimensions and m_a for both systems are summarised in Table 3. The total weight of the monolith device, including the SS-PCM sections, for 509 CPI, 734 CPI and 1225 CPI were 276 g, 311 g and 361 g, respectively.

4.2 Governing equations

4.2.1 Conservation of mass and momentum

Steady state flow profiles for each system were determined by solving the compressible steady state continuity and momentum equations. All flow conditions were laminar as the maximum Reynolds number, *Re,* in each channel was 18 for the 1225 CPI monolithic systems and

14

the maximum particle Reynolds number, Re_p, for the packed beds was 3.4. To generate the steady state profiles, pure nitrogen as an ideal gas was chosen as the bulk gas ($\rho_g = \rho_{N_2}$) and its material properties were calculated at 25 °C. The boundary and initial conditions are summarised in Table 4 and are based on a total mask gas flow rate of 50 L min^{-1} and an atmospheric outlet pressure condition. The boundary between the solid SS-PCM and the gas channel was set as a wall, using the non-slip boundary condition by setting the wall velocity, $\boldsymbol{u}_w$, to zero. For the sole purpose of generating a laminar flow profile the porous carbon and gas channel boundary was set as an impermeable wall to prevent bulk gas flow across the boundary. Within the porous carbon domain, the bulk gas velocity was set to 0 m s^{-1} i.e. permitting only diffusive species transport. Similarly, the outer packed bed casing was set as a wall. The iterations were continued until the root mean squared (RMS) residuals for mass and momentum were below 10^{-6}. The resulting flow profiles were then held constant (or frozen) and used in the transient modelling of the energy and species balance therefore removing the redundant computational cost of solving the momentum equations at each time step. The inherent assumptions of using a frozen flow profile included that the additional butane added or adsorbed and the change in temperature through the device did not significantly impact the flow profile. This is reasonable for the butane fraction and temperature ranges used within this study.

Table 4: Boundary and initial conditions required to solve the steady state continuity and momentum equations.

Packed bed			
Inlet	**Outlet**	**Impermeable wall**	**Initial condition**
$m_{z=0} = 1.3 \times 10^{-5} \text{ kg s}^{-1}$	$P_{out} = 101 \text{ kPa}$	Bed/Casing: $\boldsymbol{u}_w = 0 \text{ m s}^{-1}$	$\boldsymbol{u}_{t=0} = 0 \text{ m s}^{-1}$ $T_{g,t=0} = 25 \text{ °C}$

Monolith channel			
Inlet	**Outlet**	**Impermeable wall**	**Initial condition**
509 CPI: $m_{z=0} = 1.4 \times 10^{-8}$ kg s^{-1} 734 CPI: $m_{z=0} = 9.7 \times 10^{-9}$ kg s^{-1} 1225 CPI: $m_{z=0} = 5.8 \times 10^{-9}$ kg s^{-1}	$P_{out} = 101$ kPa	Channel/SS-PCM: $\boldsymbol{u}_w = 0$ m s^{-1} Channel/Carbon: $\boldsymbol{u}_w = 0$ m s^{-1}	$\boldsymbol{u}_{t=0} = 0$ m s^{-1} $T_{g,t=0} = 25$ °C

For the packed bed filter the porous domain was treated as a single homogenous domain encompassing both the pores and adsorbent GAC. To include the impacts of the porous domain on the flow profile the loss of momentum due to the GAC packing was included as a momentum sink term which was described by the Ergun equation, representing the isotropic loss of momentum due to viscous and kinetic effects [52,53]. Focus will be placed on presentation of the model equations for the monolith filter in the main text and all packed bed equations are described in the Supporting Information Section S2.1. The continuity (Eq. 1) and conservation of momentum (Eq. 2) equations were solved for the steady state gas flow profiles within the monolith channel domain [54].

$$\nabla \cdot \left(\rho_g \boldsymbol{u} \right) = 0 \tag{1}$$

$$\nabla \cdot \left(\rho_g \boldsymbol{u} \otimes \boldsymbol{u} \right) = -\nabla P + \nabla \cdot \left[\mu \left(\nabla \boldsymbol{u} + (\nabla \boldsymbol{u})^T - \frac{2}{3} \boldsymbol{I} (\nabla \cdot \boldsymbol{u}) \right) \right] \tag{2}$$

4.2.2   Conservation of energy

The transient thermal energy balance used to solve for the gas temperature, T_g, within the channels of the monolith is shown by Eq. 3. The thermal properties used include the bulk gas specific heat capacity, $C_{p,g}$, and thermal conductivity, λ_g. The velocity vector was obtained from the frozen flow profile obtained from the continuity and momentum equations.

16

$$\frac{\partial(\rho_g C_{p,g} T_g)}{\partial t} + \nabla \cdot (\rho_g C_{p,g} T_g \boldsymbol{u}) = \lambda_g \nabla^2 T_g \qquad (3)$$

Two conductive heat balances were solved for the porous carbon domain within the monolith. The first evaluated the T_g within the pores (Eq. 4) and the second for the solid AC temperature, T_{ac}, (Eq. 5). Due to the lack of literature regarding the pore/solid heat transfer coefficient, h_p, for phenolic resin ACs a local thermal equilibrium was maintained between the gas within the pore void and the adsorbent solid by setting a large value of h_p. Without this approximation, the heat capacity of the carbon could not be included within the model, which was deemed as an important factor for the correct assessment of the heat absorption capacity of the device. The particle porosity, ε_p, of the porous carbon was determined from helium pycnometry as described in Section S3.1 of the Supporting Information. The heat generated by butane adsorption was described within the solid phase energy balance by a volumetric energy source and the heat of adsorption, $(-\varDelta H_a)$, was evaluated from the isotherm as a fitted parameter:

$$\varepsilon_p \frac{\partial(\rho_g C_{p,g} T_g)}{\partial t} = \lambda \nabla^2 T_g - (1 - \varepsilon_p) h_p \alpha_p (T_g - T_{ac}) \qquad (4)$$

$$\frac{\partial(\rho_p C_{p,ac} T_{ac})}{\partial t} = \lambda \nabla^2 T_{ac} + h_p \alpha_p (T_g - T_{ac}) + \rho_p (-\Delta H_a) \frac{\partial q_b}{\partial t} \qquad (5)$$

The heat absorption within the pre- and post-cooler sections in the monoliths was described using a solid conductive heat transfer model (Eq. 6) where the latent heat capacity was included within an effective heat capacity, $C_{p,pcm,e}$, term [55,56].

$$\frac{\partial(\rho_{pcm} C_{p,pcm,e} T_{pcm})}{\partial t} = \lambda_{pcm} \nabla^2 T_{pcm} \qquad (6)$$

To model phase change within the heat absorbing sections, a fixed domain method [56] with local thermal equilibrium [57,58] was employed where the SS-PCM was treated as a single continuous and stationary solid. The location of phase change within the SS-PCM was predicted implicitly by defining a function for $C_{p,pcm,e}$ as shown by Eq. 7. The assumptions associated with the fixed SS-PCM domain were deemed acceptable as no visible phase change or notable change in density were observed in addition to the fact the material does not visibly flow above or below the phase change temperature [48]. The expression written for the $C_{p,pcm,e}$ included a constant sensible heat capacity, $C_{p,pcm}$, above and below the phase change temperature range and a sinusoidal function to incorporate the latent heat capacity implicitly within a smooth function. From differential scanning calorimetry (DSC) curves, which are displayed by Figure S4 in the Supporting Information, the heat absorbed via phase change occurred within a temperature range of 53 °C to 61 °C and therefore T_s and T_L were set to these respective values:

$$C_{p,pcm,e} = \begin{cases} C_{p,pcm} & T_{pcm} < T_S \\ C_{p,pcm} + \dfrac{\Delta H_L \pi}{2(T_L - T_s)} \sin\left(\pi \dfrac{T - T_L}{T_s - T_L}\right) & T_S \leq T_{pcm} \leq T_L \\ C_{p,pcm} & T_{pcm} > T_L \end{cases} \qquad (7)$$

For the transient energy balances the boundary and initial conditions are summarised in Table 5. Three domain interfaces existed for the monolith, including the gas/SS-PCM, gas/porous solid and the porous solid/SS-PCM. The gas/SS-PCM and porous solid/SS-PCM interfaces only required conservation of the heat flux, as no transport of butane occurred in these regions. The gas/porous solid interface required the conservation of both the mass and heat flux.

Inlet	Wall	Initial conditions
$T_{g,z=0} = 80\ ^\circ C$	$\lambda_g \boldsymbol{n} \cdot \nabla T_g = \lambda \boldsymbol{n} \cdot \nabla T_i$ $\lambda_g \boldsymbol{n} \cdot \nabla T_g = \lambda_{pcm} \boldsymbol{n} \cdot \nabla T_{pcm}$ $\lambda \boldsymbol{n} \cdot \nabla T_i = \lambda_{pcm} \boldsymbol{n} \cdot \nabla T_{pcm}$	$\boldsymbol{u}_{t=0} = $ Frozen profile $T_{g,t=0} = 25\ ^\circ C$ $T_{ac,t=0} = 25\ ^\circ C$ $T_{pcm,t=0} = 25\ ^\circ C$

4.2.3 Conservation of species

The species transport equations used to solve for the butane fraction, y_b, within the channels of the monolith is shown by Eq. 8. The molecular diffusion coefficient, D_m, was determined using the Chapman-Enskog correlation [59] as shown in

Table 7:

$$\frac{\partial(\rho_g y_b)}{\partial t} + \nabla \cdot (\rho_g y_b \boldsymbol{u}) = \nabla \cdot (D_m \rho_g \nabla y_b) \tag{8}$$

The species and aforementioned energy transport relationships within the porous solid were adapted and modified from previously reported numerical models which described adsorbent monolith [39] and catalytic converter [60,61] systems. The monolith walls consisted of a homogenous porous domain and the adsorptive transport within the walls was described by a diffusive transport equation using an effective pore diffusivity, D_p, derived from the Bosanquet approximation [62]. Modelling the diffusive transport directly within the AC walls approximates the transport of butane through the macropores. To mimic the microporous transport and adsorption a volumetric adsorption sink was used based on the LDF model, as described in section 4.3. The method of using separate expressions for the macropore transport and micropore

adsorption was found in literature to be commonplace in one dimensional models of packed bed adsorption using bidisperse adsorbents [53,63–66], such as activated phenolic carbons and so was adopted here:

$$\varepsilon_p \frac{\partial(\rho_g y_b)}{\partial t} = \varepsilon_p \nabla \cdot (D_p \rho_g \nabla y_b) - \rho_p M_{r,b} \frac{\partial q_b}{\partial t} \tag{9}$$

For the transient species transport balances the boundary and initial conditions are summarised in Table 6. As mentioned, the gas/porous interface required conservation of both the mass and heat flux. The mass flux described the transport of butane from the gas channels to within the pores of the adsorbent solid. Symmetry within the solution was maintained at the locations specified in Figure 3 for both the packed bed and monolith models by setting both the velocity and the scalar variable gradients normal to the plane of symmetry to zero. The correlations used to calculate the required mass and heat transport parameters are displayed in

Table 7.

Table 6: Boundary and initial conditions required to solve the transient species for the monolith system.

Inlet	Wall	Initial conditions
$y_{b,z=0} = 0.001$ 509 CPI: $m_{z=0} = 1.4 \times 10^{-8}$ kg s^{-1} 734 CPI: $m_{z=0} = 9.7 \times 10^{-9}$ kg s^{-1} 1225 CPI: $m_{z=0} = 5.8 \times 10^{-9}$ kg s^{-1}	$D_m \rho_g \boldsymbol{n} \cdot \nabla y_b = D_p \varepsilon_p \rho_g \boldsymbol{n} \cdot \nabla y_b$	$y_{b,t=0} = 0$ $\boldsymbol{u}_{t=0} =$ Frozen profile $q_{b,t=0} = 0$ mol kg^{-1}

Table 7: Correlations of molecular, Knudsen and effective pore diffusivities for the monolith system.

Diffusivities	Correlations

Molecular diffusivity [59]	$$D_m = 0.001858 \frac{T_g^{\frac{3}{2}} \sqrt{1/M_{r,N_2} + 1/M_{r,b}}}{P \sigma_{AB}^2 \Omega_{AB}}$$
Knudsen diffusivity [62]	$$D_k = \frac{d_m}{3} \sqrt{\frac{8RT_g}{\pi M_{r,b}}}$$
Effective pore diffusivity [62]	$$D_p = \left[\tau \left(\frac{1}{D_m} + \frac{1}{D_k} \right) \right]^{-1}$$

4.3 Adsorption

The rate of adsorbate uptake by the adsorbent carbon was predicted by the LDF model (Eq. 10) [67] in both the packed bed and monolith systems. In both cases, this is represented by a volumetric sink term in the gas side of the porous domain (Eq. 9). In addition, the amount of butane adsorbed, q_b, was tracked for both systems by numerically solving the LDF equation at each iteration.

$$\frac{\partial q_b}{\partial t} = k_a (q_{e,b} - q_b) \tag{10}$$

The k_a for the packed bed, as shown in Eq. 11, described the overall mass transfer coefficient including terms for film, f, macropore, m, and micropore, μ, resistances and was evaluated using the expression proposed by Farooq and Ruthven [68]. The lumped parameter approach removed the need for a separate species transport balance within the pores of the GAC which simplified the simulations:

$$k_a = \left[\left(\frac{r_p q_{b,z=0}}{3 k_f c_{b,z=0}} \right)_f + \left(\frac{r_p^2 q_{b,z=0}}{15 \varepsilon_p D_p c_{b,z=0}} \right)_m + \left(\frac{r_\mu}{15 D_\mu} \right)_\mu \right]^{-1} \tag{11}$$

The LDF coefficient for the monolith, as shown in Eq. 12, only considered the micropore resistance and was assumed to be identical to the micropore resistance term used for the packed

bed. Unlike the packed bed, which is modelled as a homogenous domain considering the interstitial gas and porous carbon in one space, the monolith model had separate domains for the gas channel and the porous carbon wall. Due to the existence of a separate carbon domain the mass transfer within the porous region could be expressed directly using a diffusive transport equation (Eq. 9) which utilised an effective pore diffusivity, D_P, to describe the impacts of molecular and Knudsen diffusion.

$$k_a = \frac{15 D_\mu}{r_\mu} \qquad (12)$$

Trace isotherm data for butane adsorption was obtained from Birkmann *et al*. [69], as displayed by Figure 4, at multiple temperatures on a microporous Norit RX 1.5 Extra AC, where they showed the Sips isotherm provided an accurate representation of the data. However, using the original Sips isotherm within the aforementioned transient equations required an infinitesimal time step to maintain numerical stability especially at low butane partial pressures, P_b, i.e. $P_b < 15$ Pa. This was attributed to the impact which the steep gradient of the isotherm curve near partial pressures of zero was having on the system of equations. For example, upon taking the gradient of the Sips isotherm the resulting equation was Eq. 13. This shows that when P_b approaches zero, as the heterogeneity constant, n, is below zero, the gradient approached infinity.

$$\frac{\partial q_{e,b}}{\partial P_b} = q_{m,b} \frac{n b_S^n P_b^{n-1}}{(1 + b_S^n P_b^n)^2} , \qquad \lim_{(P_b \to 0, \ 0 < n < 1)} \frac{\partial q_{e,b}}{\partial P_b} = \infty \qquad (13)$$

Therefore, adoption of a combined Sips/Henry isotherm, providing a linear expression in the form of the Henry isotherm at low butane partial pressures ($P_b < 15$ Pa) was used which dramatically improved stability throughout the simulation, permitting a Δt of 1.5×10^{-4} s and 2.0×10^{-4} s for

the packed bed and monolith geometries, respectively. Although this technique caused inaccuracies of the equilibrium amount of adsorbed butane, $q_{e,b}$, when compared to the experimental data, these inaccuracies were more severe for temperatures lower (i.e. 0 and 20 ºC) than the operating conditions used in this study. The non-linear regression analysis and isotherm parameters are discussed in the Supporting Information Section S2.2. The combined isotherm took the form of Eq. 14 and is displayed in Figure 4. In Eq.14 and Eq. 15, the parameter $q_{m,b}$ represented the maximum equilibrium amount of adsorbed butane and b_i described either the Henry, b_H, or Sips, b_S, affinity coefficient as a function of temperature.

$$q_{e,b} = \begin{cases} b_H P_b, & P_b < 15 \ Pa \\ q_{m,b} \dfrac{(b_S P_b)^n}{1 + (b_S P_b)^n}, & P_b > 15 \ Pa \end{cases} \tag{14}$$

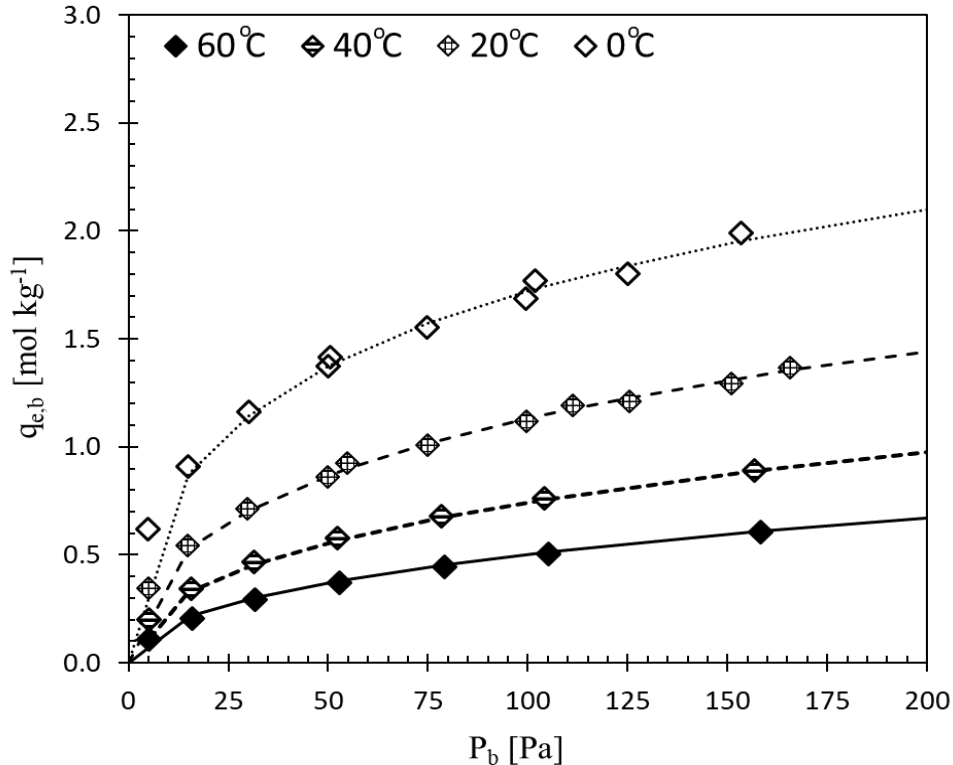$$b_i = b_{0,i} \exp\left(\frac{-\Delta H_a}{R T_g}\right) \tag{15}$$

Figure 4: Butane adsorption isotherm data at temperatures of 0 °C, 20 °C, 40 °C and 60 °C described by the combined Sips/Henry isotherm. Experimental data obtained from [69].

5. Results and Discussion

5.1 Steady state flow profiles

To validate the magnitude and profile of the axial velocity, u_z, within the monolith channel, which included the pre and post SS-PCM cooler sections, the frozen profile produced by the steady state CFD models, using the conditions outlined in Table 4, were compared against an analytical solution for square channelled flow (see Supporting Information Section S4.1). Comparisons were made under fully developed flow conditions for a total filter flow rate of 50 L min^{-1} at a length along the filter of $z = 2.5$ cm. The profile was laminar due to the small channel sizes and the maximum, $u_{z,max}$, and mean, $u_{z,mean}$, axial velocities for the 509 CPI monolith were found to be 0.41

24

m s^{-1} and 0.18 m s^{-1} compared to 0.94 m s^{-1} and 0.44 m s^{-1} for the 1225 CPI structure, respectively. The larger values of u_z in the 1225 CPI structure were due to the reduction in ε_b as the monolith channel density was increased by reducing d_{ch}. The packed bed velocity profiles exhibited a typical plug flow regime with a constant u_z across the cross section of 0.20 m s^{-1} and no-slip at the walls. These values were identical irrespective of the equivalent packed bed CPI system studied as the d_{pb} was held constant at 7.7 cm.

It is worth mentioning that the laminar flow profile within the monolith channels represented an undesirable phenomenon in relation to designing filtering devices. Although laminar regimes provide a benefit by reducing pressure drop, the $u_{z,max}$ at the channel centreline could lead to instantaneous or premature breakthroughs of both toxic gas and high temperatures, especially using higher CPI designs with low ε_b.

5.2 Pressure drop

The pressure drop as evaluated by the numerical models for monoliths with different CPIs and the equivalent mass packed bed systems are displayed in Figure 5 for a range of flow rates. For the benchmark total flow rate of 50 L min^{-1}, the 509 CPI monolith had a pressure drop of 10.4 Pa, approximately three times lower than the equivalent mass packed bed. The reduced pressure drop was due to the streamlined flow profile within the monolith channels, as opposed to the packed bed systems in which the gas traversed a tortuous path. The 734 CPI structure had a similar, albeit slightly improved pressure drop compared to the packed beds, with a pressure drop of 27.4 Pa at 50 L min^{-1}. For the 1225 CPI monolith a sharper rise in the pressure drop occurred, with a

value of 126 Pa at 50 L min^{-1}. Using the Hagen–Poiseuille equation for reference [70], the pressure drop of laminar flow in straight channels is proportional to the $u_{z,mean}$ and inversely proportional to the square of d_{ch}, which explains the significant rise in pressure drop for an incremental decrease in d_{ch}. As only L_a was changed to produce equivalent mass packed bed filters, the pressure drop only marginally increased for these systems.
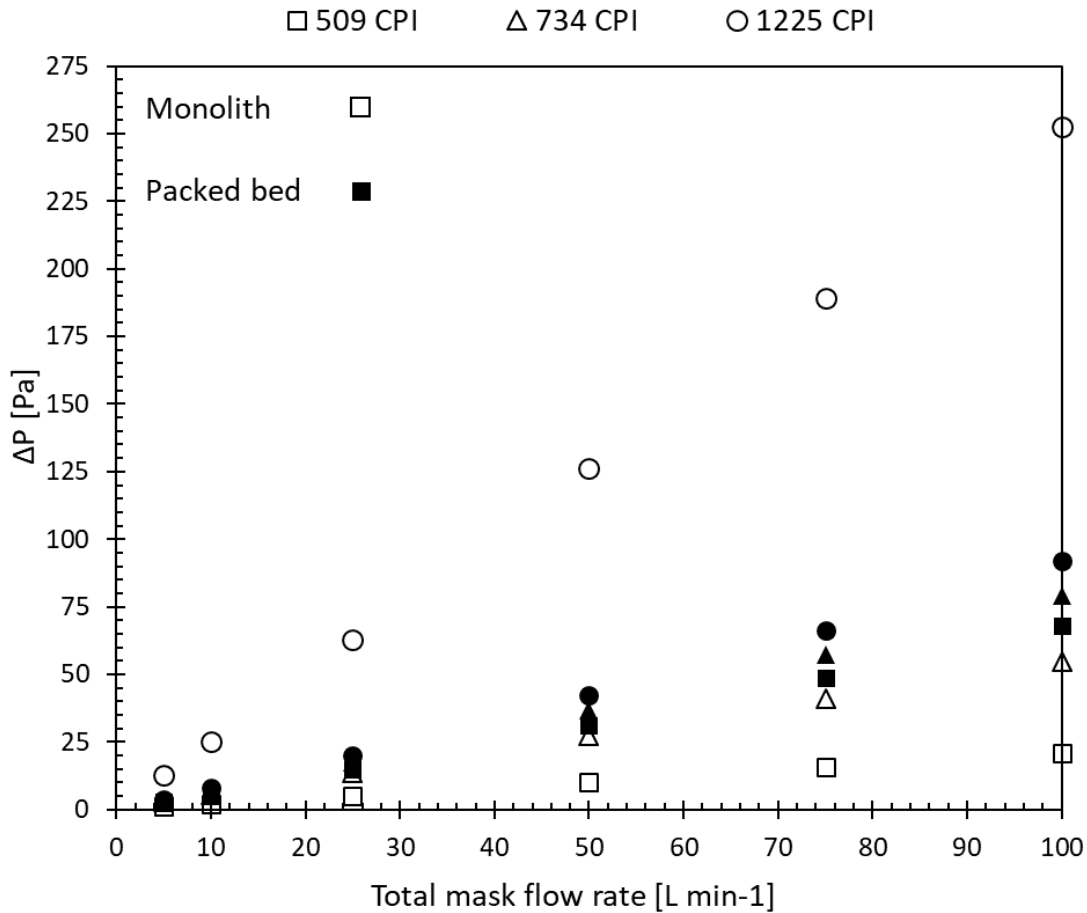

Figure 5: Pressure drop as a function of total mask flow rate for 509, 734 and 1225 CPI monoliths (open symbols) compared against equivalent mass packed beds (closed symbols). The data was for inlet conditions of 50 L min^{-1} and 25 °C.

5.3 Heat absorption

In line with the literature [11,12], an upper breathing temperature limit at the centre point of the device outlet ($x = 0$ mm, $y = 0$ mm, $z = 5.0$ cm) of 60 ºC was chosen as the condition when the device would no longer protect the user. Heat ingress from the environment and that generated by butane adsorption within the device was predominantly absorbed by utilising the latent heat of the PEG/TAIC SS-PCM within pre-cooler and post-cooler domains. Figure 6 provides a qualitative view of the T_g profile as contour lines across the XZ plane for the 509 CPI monolith design at successive use times. The impact of the velocity profile on the T_g contours is evident as the contours follow a similar laminar profile across the width of the gas channel. This highlights that the centerline of the monolith channel pertains to the highest temperature. The contours within the SS-PCM channel walls are almost flat with respect to the t_w, indicating for a $t_w/2$ of 0.2 mm or below the thermal conductivity of the SS-PCM (0.21 W m^{-1} K^{-1}) was sufficiently large to enable effective conductive heat transfer within the walls.

The temperature contour snapshots at 2 min, 8 min, 11 min and 16 min represent significant periods in relation to heat absorption within the device. At 2 min sensible heating of the device towards the mean phase change temperature of the SS-PCM, T_λ, which was approximately 57 ºC, and initial phase change at the entrance of the pre-cooler occurred. At 8 min the predominant method of heat absorption was due to the pre-cooler undergoing phase change. At 11 min the porous carbon section was undergoing sensible heating and finally at 16 min phase change within the post-cooler occurred. From the 8 min and 16 min snapshots, the phase change region can be identified by the contour between 52 - 60 ºC. Downstream, or after the point of phase change, the temperature of the device at the given snapshot remained constant which is characteristic of flows

27

cooled by phase change materials [55,57,58]. Upstream of the phase change, the device quickly

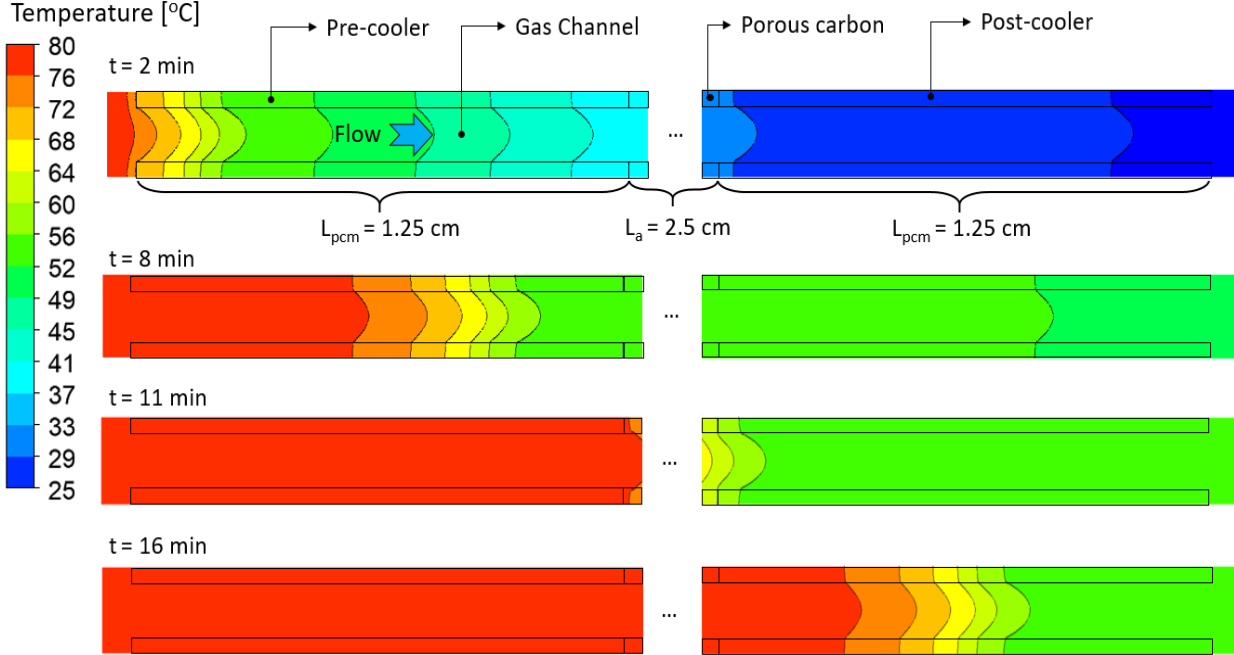heated from 60-80 °C, as only sensible heat remained.

Figure 6: Contour plots of the temperature on the XZ plane, including temperature profiles within the gas channel and SS-PCM walls. These plots are for inlet conditions of 50 L min^{-1}, 1000 ppm & 80 °C.

The $C_{p,pcm,e}$ and $C_{p,ac}$ (denoted as $C_{p,i}$) within the solid SS-PCM and porous carbon walls and

the T_g at the centerline are plotted in Figure 7 (a) as a function of filter length for various use times.

This indicates the locations of phase change within the pre- and post-cooler sections and its impact

on the centerline T_g. Phase change within the SS-PCM corresponded with sinusoidal type peaks in

the $C_{p,pcm,e}$ and heels in the T_g curves, followed by an almost flat T_g profile along the centerline

length. For example, at 8 min, the maximum $C_{p,pcm,e}$ occurs at $z \approx 1.0$ cm followed by a subsequent

heel in the T_g curve, after which the T_g was maintained at $\sim T_\lambda$. This finding was in good agreement

with the T_g contours in Figure 6. The shape of the $C_{p,pcm,e}$ curves were well defined throughout the

device, with a sharp rise to the maximum (26,100 J kg^{-1} K^{-1}) corresponding to a T_{pcm} of 57 °C, with

28

an extended tail after the maximum point, which indicated a slower increase in T_{pcm} from 53 °C to 57 °C. At 18 min the heel in the T_g curve occurred at the end of the post cooler section indicating that at approximately this time the latent heat had been utilised. Indeed, after this time, the remainder of the device heated rapidly to 80 °C.

Figure 7 (b) displays the T_g at the monolith channel centre (x = 0 mm, y = 0 mm), or worst case T_g, as a function of filter length and use time for the 509 CPI mask design. Importantly, this figure provides further granularity regarding the time when the T_g within the porous carbon section rose above T_λ. By 10 min the sensible and latent heat of the SS-PCM in the pre-cooler section had been utilised and sensible heating of the gas within the porous carbon section occurred, as evidenced by the onset of a temperature increase in the porous carbon section. The heating of the porous carbon represented an important step during the filtration process as this reduced the adsorbents capacity for the adsorbate, explained in section 5.4, leading to desorption of butane. By 12 min the T_g within the adsorbent carbon section had reached ~80 °C and the latent heat of SS-PCM within the post-cooler section started to be utilised in order to hold the outlet T_g below 60 °C. Therefore, for low concentrations of a single component adsorbent, without chemical oxidation, the proposed monolith filter provided breathable temperatures for up to 18 min. However, it is unlikely that the device inlet temperature will constantly be held at 80 °C as the user tries to escape a burning building and so the new design should provide adequate protection from high inhalation temperatures.
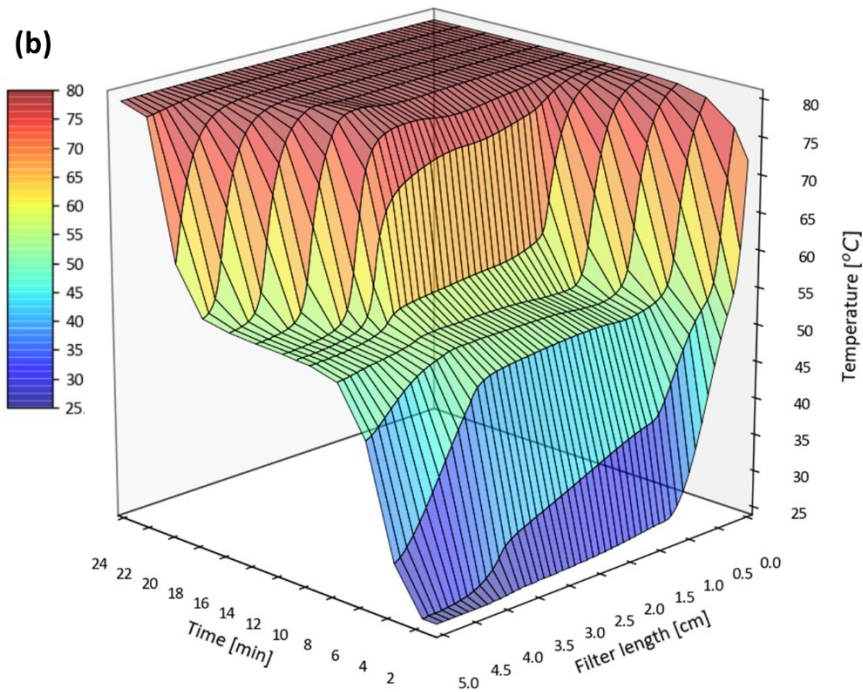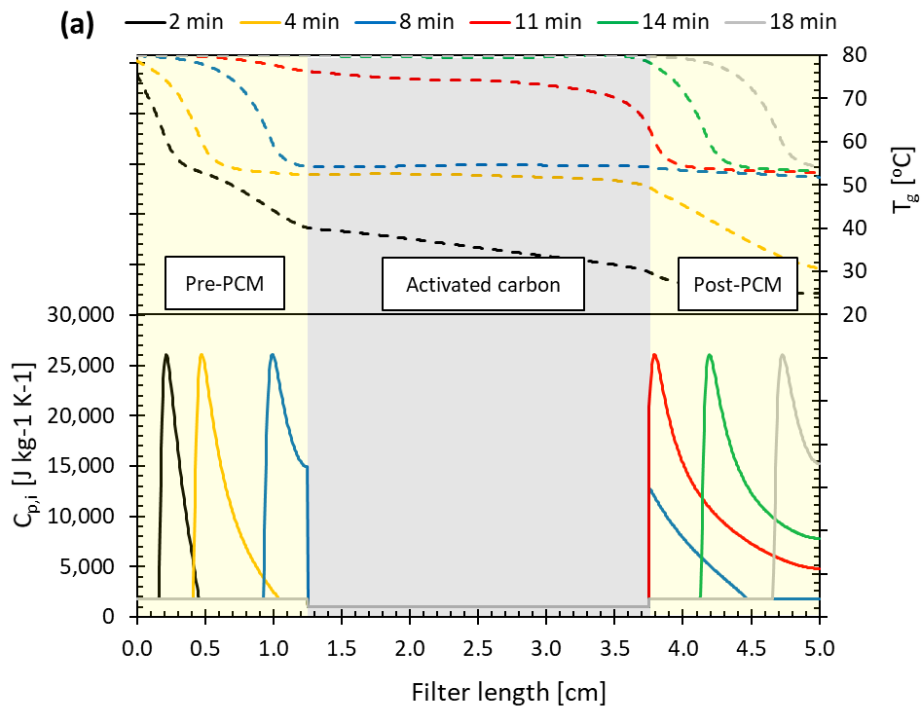
*Figure 7: **(a)** Heat capacity within the solid phases (x = 0.45 mm, y = 0 mm) and gas temperature at the centerline (x = 0 mm, y = 0 mm) along the filter length at various times and **(b)** the full gas temperature profile of the gas phase along the channel centerline (x = 0 mm, y = 0 mm) for the 509 CPI mask. Both plots are for inlet conditions of 50 L min^{-1}, 1000 ppm and 80 °C.*

5.4 Adsorption

Figure 8 provides a qualitative view of the y_b profile as contour lines across the XZ plane at different use times for the 509 CPI monolith. The impact of the velocity profile on the y_b contours is again evident as the contours followed a laminar profile across the width of the gas channel. Once more, the centerline of the channel pertained to the most dangerous conditions. The transport of butane within the pores of the monolith wall, which was purely diffusive as described by the diffusive flux term $[\varepsilon_p \nabla \cdot (D_p \rho_g \nabla y_b)]$ in Eq. 9, combined with butane sink term was also depicted, shown by the value of y_b decreasing towards the outer wall symmetry.

The y_b contour snapshots at 2 min, 8 min, 11 min and 16 min represent significant periods in relation to butane adsorption within the device. The snapshot at 2 min represents initial introduction of butane into the porous carbon section and the development of the mass transfer zone. By 8 min, the mass transfer zone was fully developed and spanned a length of $\approx$ 0.8 cm. The T_g within the porous carbon at this time was $\sim T_\lambda$ and even before this snapshot remained relatively constant due to the heat absorption within the pre-cooler. Holding the porous carbon at a constant temperature also maintained a constant $q_{e,b}$ for a given P_b. The inclusion of a heat absorbing component therefore permitted more adsorbate to be held within the porous carbon. At 11 min, the latent heat within the pre-cooler had been utilised and the T_g within the porous carbon section began to increase from T_λ to 80 °C. This temperature change caused the formation of adsorption and desorption zones as the $q_{e,b}$ for a given P_b was reduced, which in some locations reversed the LDF sink (Eq.10) as q_b was higher than $q_{e,b}$. The rapid reduction in $q_{e,b}$ due to heating caused a peak in y_b within the device of $\sim$ 2200 ppm. At 16 min, the Tg within the carbon was $\sim$80 °C and the mass transfer zone had reached the end of the porous carbon section. A desorption zone

was still present, but with a less severe peak in y_b due to convection of butane out of the device
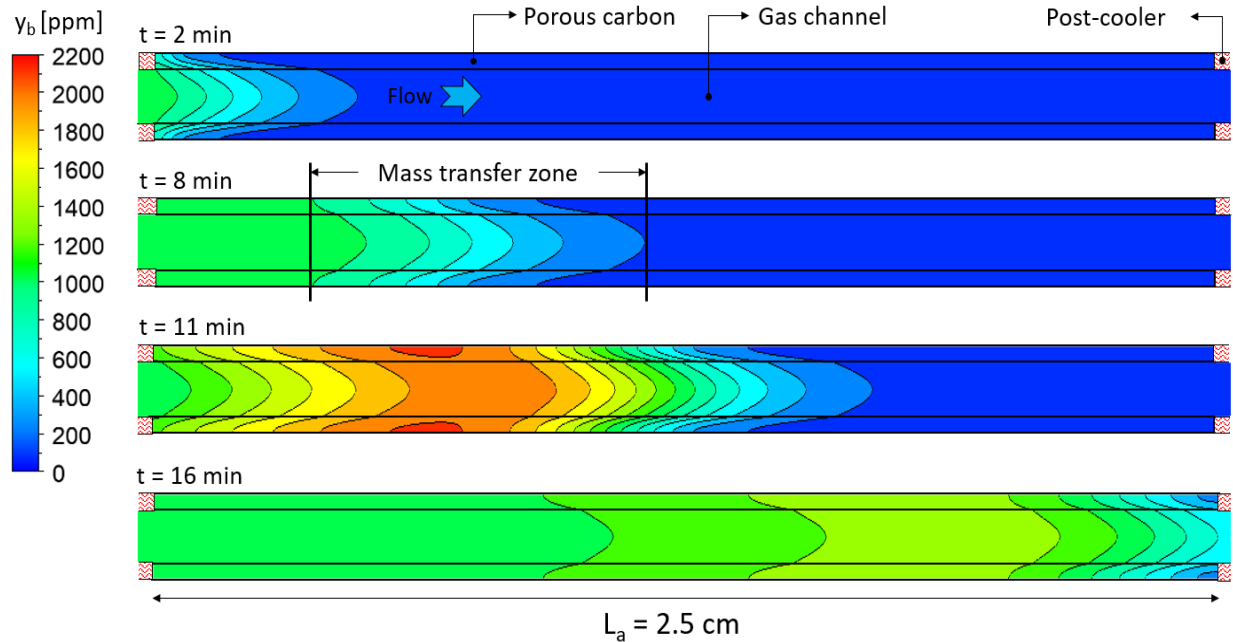
and downstream adsorption.

Figure 8: Contour plots of the butane fraction on the XZ plane, including butane profiles within the gas channel and porous carbon walls for the 509 CPI mask. These plots are for inlet conditions of 50 L min^{-1}, 1000 ppm and 80 ^oC.

Several breakthrough times were defined in accordance with the BS EN 403 standards [13]

which specifies the minimum allowable breakthrough fractions after 15 minutes of use for gases

including acrolein, HCl, HCN and CO. The breakthrough fractions of these gases are 0.5 %, 0.5

%, 2.5 % and 8.0 % of the inlet fraction, respectively. Therefore, breakthrough times were defined

as the time for the y_b at the filter outlet ($x = 0.0$ cm, $y = 0.0$ cm and $z = 5.0$ cm) to exceed 5 ppm,

$t_{b,0.005}$, 25 ppm, $t_{b,0.025}$, and 80 ppm, $t_{b,0.080}$, respectively. In addition, the time to reach equilibrium,

$t_{e,0.95}$, was defined as the time for y_b to exceed 950 ppm. These results are displayed in Table 8 and

confirm that instantaneous breakthrough was not found in either the monolith or packed bed filters

as $t_{b,0.005}$ was above 0.00 min. The difference between $t_{e,0.95}$ and $t_{b,0.005}$ gives a good indication of

32

the time for the mass transfer zone to pass through the device outlet, t_{mtz}, where a shorter time indicated an improved mass transfer of butane within the filter. The best performing filter in terms of adsorption was the 1225 CPI monolith which contained the most carbon and the smallest channels. This permitted the longest breakthrough time in all cases and the shortest mass transfer zones. The values of t_b for each CPI were all greater and the mass transfer zones were shorter than their equivalent packed bed system, indicating improved adsorption performance. Although the monolith filter had improved breakthrough times when compared to the packed bed systems, this advantage diminished with increased outlet fraction. For example, the 734 CPI monolith filter increased $t_{b,0.005}$ by 84% and $t_{b,0.080}$ by 23%, compared to the packed bed filter. This was attributed to the sharp breakthrough curve exhibited by the monolith filters. All of the monolith filters concentrated the outlet stream due to the periodic increase in adsorbate capacity within the device, as shown by Figure 9, which displays the fraction of butane surpassing the $y_{b,z=0}$ of 1000 ppm. Although the user of an FEM with a monolithic filter may benefit from a longer use time, there is an eventual concentration of the toxic species at the outlet, due to the heat changes within the device causing desorption.

Table 8: Breakthrough and equilibrium times for various monolith CPIs and equivalent packed bed systems.

	Monolith			Packed bed		
	509 CPI	734 CPI	1225 CPI	$L_a = 2.5$	$L_a = 2.9$	$L_a = 3.4$
$t_{b,0.005}$ [min]	11.2	13.5	17.0	5.33	7.33	9.21
$t_{b,0.025}$ [min]	12.7	14.8	18.3	8.00	10.1	12.6
$t_{b,0.080}$ [min]	13.9	15.9	19.4	10.5	12.9	15.6
$t_{e,0.95}$ [min]	17.1	18.8	22.3	24.4	27.4	30.7
t_{mtz} [min]	5.90	5.30	5.30	19.1	20.1	21.5

The equivalent packed bed systems exhibited a more conventional breakthrough curve, as y_b approached 1000 ppm and did not exceed this level. The packed bed breakthrough curves were shallow in comparison to the monolith curves which led to mass transfer zones which were longer in duration and shorter breakthrough times. Similar behavior was reported by Valdes-Solis *et al.* [71], who investigated carbon packed bed (cylindrical packing, $d_p = 0.94$ mm) and monoliths (200-900 CPI) and found that monoliths delay the breakthrough of low concentrations of toxic species, as exhibited by the greater breakthrough times in this study. Two factors were identified that could have attributed to the reduced adsorption performance. Firstly, the packed bed model used a global k_a (Eq. 11), combining the film, macropore and micropore resistances which had values of 26.9 s, 30.4 s and 6.67 s at $T_g = 80$ °C, respectively. Therefore, the film and macropore resistances were more significant which was partly determined by the packing d_p. The film and macropore resistances could be reduced, therefore improving the rate of adsorbate uptake, by reducing the packing d_p which features in these terms. However, this would be at the determinant of pressure drop. For example, using a d_p of 0.30 mm would provide film and macropore resistance of 3.65 s and 2.74 s, but increase the pressure drop to ~380 Pa for the conditions used in this paper. Secondly, as already explained the monolith filter had a periodic increase in adsorbate capacity. This occurred between 1.4-11 min, which is the range of time when the temperature of the packed bed system was at 80 °C and the temperature of the monoliths carbon section was held at T_λ. Between this period the maximum $q_{e,b}$ for the packed bed and monolith was 0.25 mol kg^{-1} and 0.40 mol kg^{-1}, respectively, indicating the packed bed capacity for butane was lower leading to a quicker breakthrough.
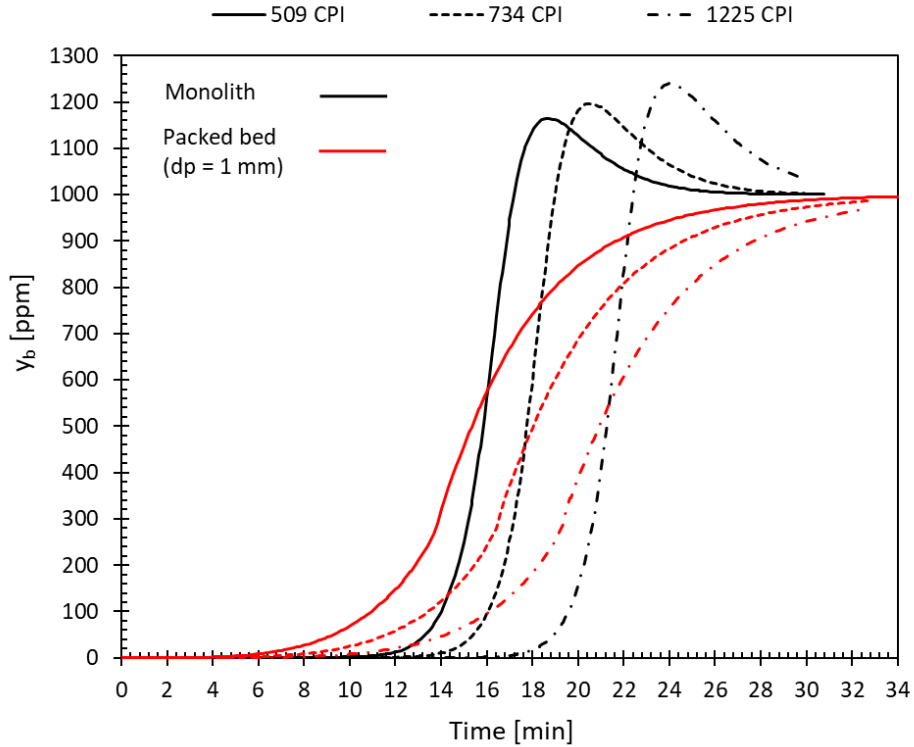
Figure 9: Butane breakthrough curves for 509, 734 & 1225 CPI monoliths compared against equivalent CPI packed beds. This plots was for inlet conditions of 50 L min⁻¹, 1000 ppm and 80 °C.

Figure 10 and Figure 11 provide further clarity on the impact that the addition of heat absorbing components had on the adsorption performance within the monolith device. Upon reaching approximately 10 min, y_b within the gas channel of the adsorbent section (1.25 cm $< z <$ 3.75 cm) began to rapidly rise above the inlet butane concentration of 1000 ppm, as shown by the 1200 ppm contour in Figure 10. This occurred as the T_g within the porous carbon increased, which reduced the $q_{e,b}$ as outlined in the isotherm expression (Eq. 14-15). The gas within the carbon heated from T_λ to 80 °C within 2 minutes after the latent heat capacity within the SS-PCM pre-cooler was utilised. The rapid increase in T_g caused the desorption of butane back into the gas channel, as $q_{e,b}$ was lower than q_b in the gas sink expression (Eq. 9). The rapid reduction in available adsorbate capacity led to a maximum y_b value of 2000 ppm within the gas channel

centerline, and 2200 ppm within the porous carbon wall at 11 minutes, as displayed in Figure 8. Although there was a concentration in the outlet y_b when compared to the inlet butane fraction, $y_{b,z=0}$, due to the advection of butane through the device and the available adsorbate capacity downstream of the y_b peak, the y_b at the outlet of the device did not exceed 1200 ppm.
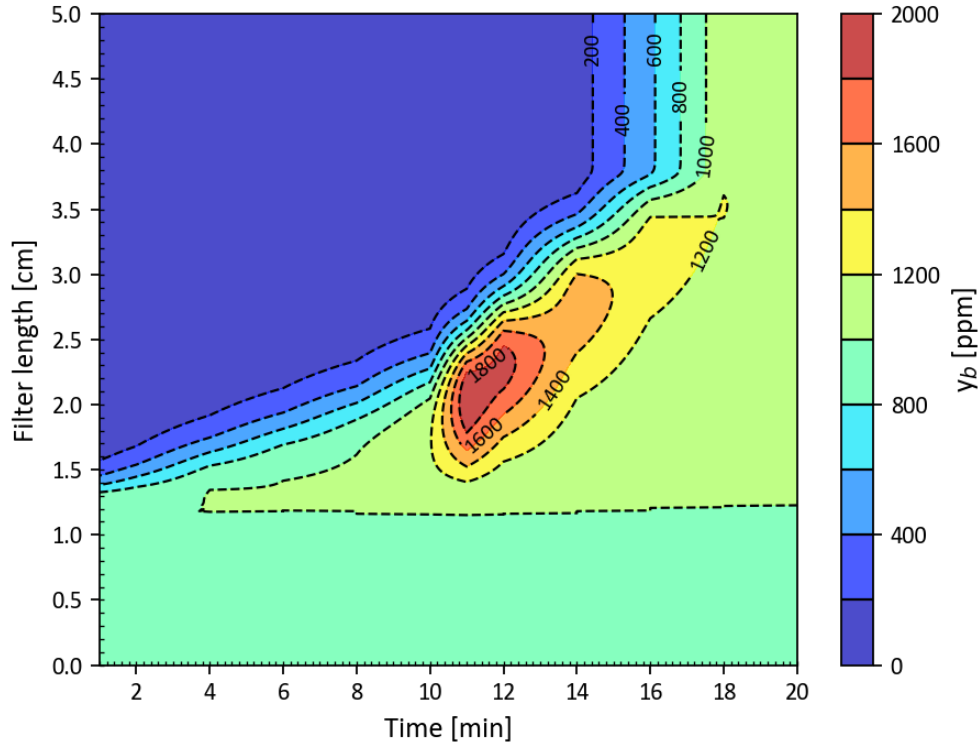

Figure 10: Butane fraction at the channel centerline (x = 0 mm, y = 0 mm) along the filter length at various times for 20 minutes of use for the 509 CPI mask. This plot was for inlet conditions of 50 L min⁻¹, 1000 ppm & 80 °C.

Figure 11 shows the q_b as a function of filter length for different device use times. The value of q_b depends on the LDF rate expression (Eq. 12) as it approaches the value of $q_{e,b}$ at a rate determined by k_a. The change of $q_{e,b}$ during the simulations was determined by P_b (or y_b) and T_g, as all other parameters used to evaluate the isotherm were held constant. A consistent maximum of 0.40 mol kg⁻¹ was reached near the entrance of the porous carbon section which corresponded to a y_b of 1000 ppm and a T_g of T_λ. This consistent maximum was maintained due to the heat

36

absorption within pre-cooler PCM holding the T_g within the AC pores reasonably constant. At 10 min, the T_g within the carbon began heating above T_λ which began reducing q_b. By 14 min q_b was below 0.3 mol kg^{-1} at most locations within the porous wall. The rapid reduction in adsorbate capacity within the carbon at 10-12 min near the entrance of the porous carbon section corresponded with the peak of y_b within the channel centerline due to the butane desorption, as displayed in Figure 10. Note that a brief and greater maximum occurs between 1-3 min at the entrance of the porous carbon wall ($L_a \sim 0.0$ cm), where the value of q_b was above 0.45 mol kg^{-1} because at this time T_g was lower than T_λ and the y_b was 1000 ppm.
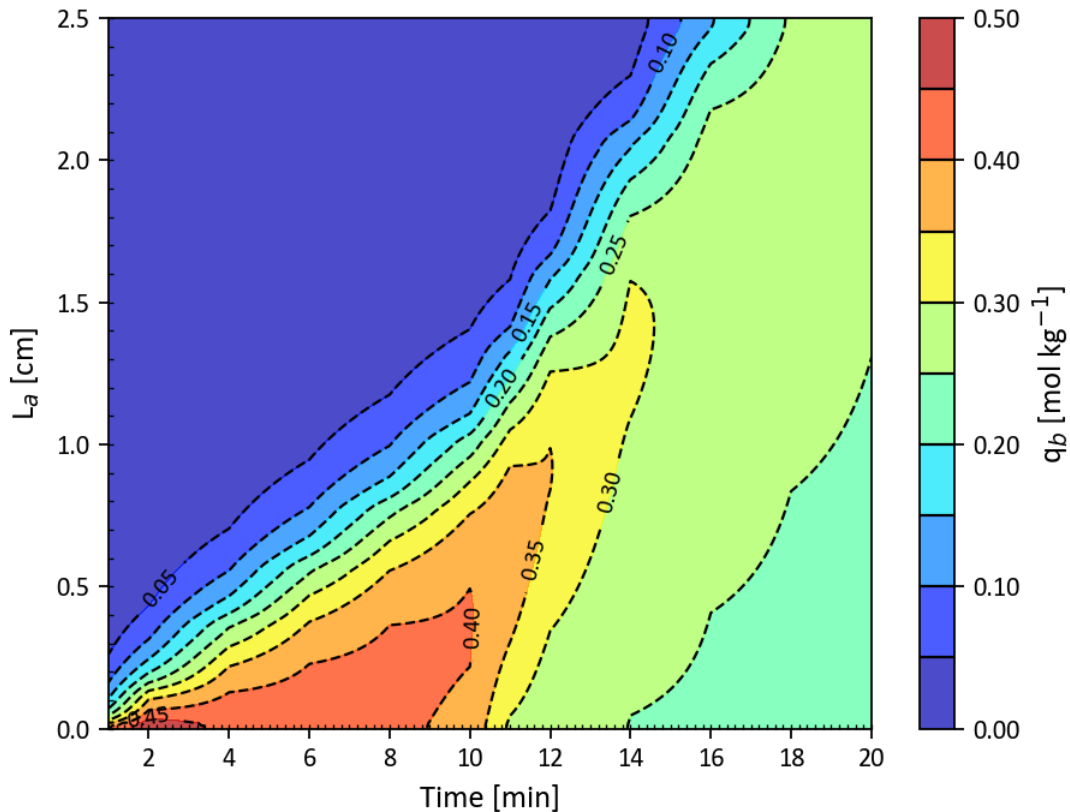

Figure 11: Amount of butane adsorbed within the porous carbon wall (x = 0.45 mm, y = 0 mm) along the adsorbent length at various times for 20 minutes of use for the 509 CPI mask. This plot was for inlet conditions of 50 L min^{-1}, 1000 ppm & 80 °C.

This indicated that the inclusion of a heat absorbing component provided a periodic advantage with respect to adsorbate capacity within the porous carbon, resulting in improved adsorption performance. This finding also highlighted that the length of the pre- and post-cooler sections could be further fine-tuned. Increasing the relative size of the pre-cooler would provide a longer period of increase adsorbate capacity within the carbon. However, when a larger quantity of adsorptives or reactants are present in the incoming gas stream the generated process heats would rise. This would require a more complex, multicomponent model to assess the impacts of high quantities of toxic species to correctly assess the heat absorption required at each cooler section.

The figures for the equivalent packed bed system are shown in the Supporting Information Section S4.2. These designs do not have any heat absorption capabilities and, for example, the T_g at all locations within the equivalent 509 CPI packed bed filter was found to increase to 80 °C after approximately 1.4 min, as opposed to 12 min for the monolithic device. This shows the heat absorbent capabilities of commercial packed bed FEMs is negligible. Therefore, there was no periodic regions of increased adsorbate capacity and the butane profiles within the packed bed designs are more conventional in shape.

6. Recommendations

The optimal monolithic FEM contained monoliths with a density of 734 CPI. The design improved the breathing burden with a pressure drop of 27.4 Pa i.e. lower than all the equivalent mass packed bed systems investigate here. The inhalation temperature was held below 60 °C for 22 min and the most stringent butane breakthrough time of $t_{b,0.005}$ was approximately 14 min. These

improved values compared to the 509 CPI monoliths are largely due to an increase in latent heat and adsorbate capacity due to a lower ε_b for the 734 CPI device. The mass transfer of butane within the 734 CPI monolith was also superior compared to the equivalent packed bed, as evident from the t_{mtz} values of 5.30 min compared to 20.1 min, respectively. Although the 1225 CPI had improved values of temperature protection and breakthrough time, the pressure drop was higher at 126 Pa and the peak y_b value at the device outlet, due to periodic butane desorption, was higher.

By using a heat absorbing SS-PCM the proposed technology provided thermal protection above the minimal required use time of 15 min. The numerical model provided new insights with respect to the impact of using an heat absorbing SS-PCM preceding an adsorbent, as summarised by the findings in Figure 9, Figure 10 and Figure 11. Use of an SS-PCM in this way holds an adsorbent at a constant temperature as long as latent heat capacity remains, which maintains a higher and constant $q_{e,b}$ at a given P_b. However, upon utilisation of the latent heat capacity of the SS-PCM the adsorbent quickly heats and desorption occurs, which concentrates the outlet stream beyond the inlet concentration of adsorptive. This study for a novel type of FEM provides new insights to the opportunity to improve respiratory protection equipment for numerous applications by reducing inhalation burden, improving adsorption performance and including the ability to absorb heat, protecting the user from inhalation burns.

7. Conclusions

A new type of filtering device has been proposed for implementation in an FEM. The new design improves upon commercial design, using a square channeled monolithic structure to reduce pressure drop and the inclusion of heat absorbing components in the form of SS-PCMs to remove environmental and process heats. The pressure drop was three times lower for the 509 CPI monoliths compared to the equivalent mass packed bed. Based on the modelling studies the use of a pre- and post-cooler SS-PCM section protected the user from an 80 °C inlet temperature at a constant total mask flow rate of 50 L min^{-1} for a minimum of 18 min. The use of heat absorbing components within the monolithic filter provided a periodic increase in the adsorbate capacity as the porous carbon section was held at T_λ as opposed to the packed bed systems which heated rapidly to 80 °C. However, once the latent heat within the pre-cooler section was utilised a rapid increase in T_g occurred within the porous carbon region. This produced y_b values at the outlet above the $y_{b,z=0}$ as desorption zones were formed within the device due to a reversal in the LDF sink as q_b was higher than $q_{e,b}$. The optimum design was cartridges containing the 734 CPI monoliths, which maintained a pressure drop lower than all the packed bed designs, a breathing temperature below 60 °C for 22 min and a $t_{b,0.005}$ of approximately 13.5 min. Further development to the numerical model would include expressions to describe multicomponent adsorption and chemical oxidation of the more toxic species, such as CO. It is expected that the length of the pre- and post-cooler sections will be dependent on the highly exothermic oxidation of CO and can be tailored based on expected toxic gas inlet concentrations.

Acknowledgements

Declaration of Competing Interest

The authors declare that they have no known competing financial interests or personal relationships that could have appeared to influence the work reported in this paper.

Appendix A. Supporting Information

Supplementary information to this article can be found online at <URL>.

Nomenclature

Symbol	Description	SI Unit
Roman		
b_H	Henry affinity coefficient	Pa^{-1}
b_i	General affinity coefficient	Pa^{-1}
b_S	Sips affinity coefficient	Pa^{-1}
$c_{b,z=0}$	Butane inlet concentration	$mol\ m^{-3}$
$C_{p.ac}$	Activated carbon specific heat capacity	$J\ kg^{-1}\ K^{-1}$
$C_{p,g}$	Gas specific heat capacity	$J\ kg^{-1}\ K^{-1}$
$C_{p,pcm}$	SS-PCM specific heat capacity	$J\ kg^{-1}\ K^{-1}$
$C_{p,pcm,e}$	Effective SS-PCM specific heat capacity	$J\ kg^{-1}\ K^{-1}$
d_{ch}	Channel width/height	m
d_m	Macropore diameter	m

d_p	Particle diameter	m
d_{pb}	Packed bed diameter	m
D_k	Knudsen diffusion	$m^2\,s^{-1}$
D_M	Molecular diffusivity	$m^2\,s^{-1}$
D_p	Pore diffusivity	$m^2\,s^{-1}$
D_μ	Micropore diffusivity	$m^2\,s^{-1}$
h_p	Pore/solid mass transfer coefficient	$W\,m^{-2}\,s^{-1}$
$(-\Delta H_a)$	Heat of adsorption	$J\,mol^{-1}$
$(-\Delta H_L)$	SS-PCM latent heat capacity	$J\,kg^{-1}$
$\boldsymbol{I}$	Identity matrix	-
k_a	Linear driving force coefficient	s^{-1}
k_f	Film mass transfer coefficient	$m\,s^{-1}$
L_a	Adsorbent length	m
L_e	Entrance/exit length	m
L_{pcm}	PCM length	m
m_a	Adsorbent mass	kg
$m_{z=0}$	Inlet mass flow rate	$kg\,s^{-1}$
$M_{r,i}$	Molecular weight of component i	$kg\,mol^{-1}$
n	Heterogeneity constant	-
$\boldsymbol{n}$	Unit normal vector	-
P	Pressure	Pa
P_b	Butane partial pressure	Pa
P_{out}	Outlet pressure condition	Pa
q_b	Amount of adsorbed butane	$mol\,kg^{-1}$
$q_{b,t=0}$	Initial amount of adsorbed butane	$mol\,kg^{1}$
$q_{b,z=0}$	Amount of adsorbed butane at $c_{b,z=0}$ & $T_{g,z=0}$	$mol\,kg^{1}$

$q_{e,b}$	Equilibrium amount of adsorbed butane	mol kg^{-1}
$q_{m,b}$	Maximum equilibrium amount of adsorbed butane	mol kg^{-1}
r_p	Particle radius	m
r_μ	Microparticle radius	m
R	Universal gas constant	J mol^{-1} K^{-1}
Re	Reynolds number	-
Re_p	Particle Reynolds number	-
$t_{b,0.005}$, $t_{b,0.025}$, $t_{b,0.080}$	Breakthrough time	s
$t_{e,0.95}$	Equilibrium time	s
t_{mtz}	Mass transfer zone delta	s
t_w	Wall thickness	m
T_{ac}	Activated carbon temperature	K
$T_{ac,t=0}$	Initial activated carbon temperature	K
T_g	Gas temperature	K
$T_{g,t=0}$	Initial gas temperature	K
$T_{g,z=0}$	Inlet gas temperature	K
T_{pcm}	SS-PCM temperature	K
$T_{pcm,t=0}$	Initial SS-PCM temperature	K
T_λ	Mean SS-PCM phase change temperature	K
u_z	Axial velocity	m s^{-1}
$u_{z,max}$	Maximum axial velocity	m s^{-1}
$u_{z,mean}$	Mean axial velocity	m s^{-1}
$\boldsymbol{u}$	Superficial velocity vector	m s^{-1}
$\boldsymbol{u}_{t=0}$	Initial velocity vector	m s^{-1}
$\boldsymbol{u}_w$	Wall velocity vector	m s^{-1}
y_b	Butane fraction	-

$y_{b,t=0}$	Initial butane fraction	-
$y_{b,z=0}$	Inlet butane fraction	-

Greek

α_p	Pore/solid specific surface area	m^{-1}
ε_b	Bulk (channel) voidage	-
ε_p	Particle voidage	-
ρ_b	Adsorbent bulk density	$kg\ m^{-3}$
ρ_g	Bulk gas density	$kg\ m^{-3}$
ρ_{N2}	Nitrogen density	$kg\ m^{-3}$
ρ_P	Particle density	$kg\ m^{-3}$
ρ_{pcm}	SS-PCM density	$kg\ m^{-3}$
ρ_s	Skeletal density	$kg\ m^{-3}$
λ	Porous thermal conductivity	$W\ m^{-1}\ K^{-1}$
λ_g	Bulk gas thermal conductivity	$W\ m^{-1}\ K^{-1}$
λ_{pcm}	SS-PCM thermal conductivity	$W\ m^{-1}\ K^{-1}$
μ	Bulk gas viscosity	Pa s
σ_{AB}	Collision diameter	m
τ	Pore tortuosity	-
Ω_{AB}	Collision function	-

References

[1] Home Office, Fire and rescue incident statistics, 2019.

[2] U.S. Fire Administration, Civilian Fire Fatalities in Residential Buildings (2013-2015), Emmitsburg, 2017. https://www.usfa.fema.gov/data/statistics/ (accessed January 3, 2019).

[3] Home Office, Fire statistics: Fatalities from fires by cause of death (0504), (2019). https://www.gov.uk/government/statistical-data-sets/fire-statistics-data-tables (accessed December 13, 2019).

[4] S.J. Chong, Y.O. Kok, R.X.Y. Tay, D.S. Ramesh, K.C. Tan, B.K. Tan, Quantifying the impact of inhalational burns: a prospective study, Burn. Trauma. 6 (2018) 1–10.

https://doi.org/10.1186/s41038-018-0126-z.

[5]   C.M. Ryan, D.A. Schoenfeld, W.P. Thorpe, R.L. Sheridan, E.H. Cassem, R.G. Tompkins, Estimates of the probability of death from burn injuries, N. Engl. J. Med. 338 (1998) 362–366. https://doi.org/10.1056/nejm199806183382514.

[6]   CTIF: International association of fire and rescue services, World Fire Statistics, 2018.

[7]   Sundström, Sundström SR77-3 escape hood, (2016). http://www.sea.com.au/sund/prod_sr77_3.html (accessed May 5, 2020).

[8]   M.S. Levine, E.P. Radford, Fire victims: Medical outcomes and demographic characteristics, Am. J. Public Health. 67 (1977) 1077–1080. https://doi.org/10.2105/AJPH.67.11.1077.

[9]   Health and Safety Executive, EH40/2005 Workplace exposure limits, 2018.

[10]   G. Rein, X. Zhang, P. Williams, B. Hume, A. Heise, A. Jowsey, B. Lane, J.L. Torero, Multi-Storey Fire Analysis for High-Rise Buildings, in: 11th Interflam, 2007.

[11]   C. Cossell, J. Ma, S. Spindel, Y. Wang, Tracheal Burning From Hot Air Inhalation, 2007.

[12]   D.A. Purser, Toxic product yields and hazard assessment for fully enclosed design fires, Polym. Int. 49 (2000) 1232–1255. https://doi.org/10.1002/1097-0126(200010)49:10<1232::AID-PI543>3.0.CO;2-T.

[13]   Technical Committee CEN/TC 79, BS EN 403:2004. Respiratory protective devices for self-rescue - Filtering devices wtih hood for escape from fire - Requirements, testing, marking, (2004).

[14]   J. Szeinuk, W.S. Beckett, N. Clark, W.L. Hailoo, Medical evaluation for respirator use, Am. J. Ind. Med. 37 (2000) 142–157. https://doi.org/10.1002/(SICI)1097-0274(200001)37:1<142::AID-AJIM11>3.0.CO;2-K.

[15]   Dräger, Dräger PARAT® 7500 Filtering Escape Hoods, (2020). https://www.draeger.com/en_uk/Products/PARAT-7500 (accessed May 5, 2020).

[16]   D.A. Purser, Asphyxiant components of fire effluents, in: A.A. Stec, R. Hull (Eds.), Fire Toxic., Woodhead, Cambridge, 2010: pp. 118–198. https://doi.org/10.1533/9781845698072.

[17]   D.A. Purser, The evolution of toxic effluents in fires and the assessment of toxic hazard, Toxicol. Lett. 65 (1992) 247–255.

[18]   D.A. Purser, Hazards from smoke and irritants, in: A.A. Stec, R. Hull (Eds.), Fire Toxic., Woodhead, Cambridge, 2010: pp. 51–117.

[19]   D.A. Purser, Combustion Toxicity, in: M.J. Hurley et al (Ed.), SFPE Handb. Fire Prot. Eng., fifth, Springer, New York, 2016: pp. 2207–2307.

[20]   Y. Alarie, Toxicity of Fire Smoke, Crit. Rev. Toxicol. 32 (2002) 259–289. https://doi.org/10.1080/20024091064246.

[21]   R.J. Crewe, A.A. Stec, R.G. Walker, J.E.A. Shaw, T.R. Hull, J. Rhodes, T. Garcia-Sorribes, Experimental Results of a Residential House Fire Test on Tenability: Temperature, Smoke, and Gas Analyses, J. Forensic Sci. 59 (2014) 139–154. https://doi.org/10.1111/1556-4029.12268.

[22]   N. Traina, G.P. Horn, S. Kerber, D.C. Kyritsis, Occupant Tenability in Single Family Homes: Part I-Impact of Structure Type, Fire Location and Interior Doors Prior to Fire Department Arrival, Fire Technol. 53 (2017) 1589–1610. https://doi.org/10.1007/s10694-017-0651-5.

[23]   S. Dey, G.C. Dhal, D. Mohan, R. Prasad, Ambient temperature complete oxidation of carbon monoxide using hopcalite catalysts for fire escape mask applications, Adv. Compos. Hybrid Mater. 2 (2019) 501–519. https://doi.org/10.1007/s42114-019-00108-5.

[24]   G.K. Prasad, B. Singh, R. Vijayaraghavan, Respiratory protection against chemical and biological warfare agents, Def. Sci. J. 58 (2008) 686–697. https://doi.org/10.14429/dsj.58.1692.

[25]   W.M.T.M. Reimerink, The use of activated carbon as catalyst and catalyst carrier in industrial applications, Elsevier Masson SAS, 1999. https://doi.org/10.1016/s0167-2991(99)80571-0.

[26]   J.F. Richardson, J.H. Harker, J.R. Backhurst, Adsorption, in: Part. Technol. Sep. Process., fifth, Elsevier, 2002.

[27]   J.A. Menéndez-Díaz, I. Martín-Gullón, Types of carbon adsorbents and their production, Act. Carbon Surfaces Environ. Remediat. (2006) 1–48.

[28]   X. Xie, Y. Li, Z.Q. Liu, M. Haruta, W. Shen, Low-temperature oxidation of CO catalysed by Co3O4 nanorods., Nature. 458 (2009) 746–749. https://doi.org/10.1038/nature07877.

[29]   M. Haruta, S. Tsubota, T. Kobayashi, H. Kageyama, M.J. Genet, B. Delmon, Low-Temperature Oxidation of CO over Gold Supported on TiO2, a-Fe2O3 and Co3O4, J. Catal. 144 (1993) 175–192.

[30]   United States Department of Labor: Occupational Safety and Health Adminstration, OSHA Technical Manual (OTM) | Section VIII: Chapter 2: Respiratory Protection, (1999). https://www.osha.gov/dts/osta/otm/otm_viii/otm_viii_2.html (accessed July 1, 2020).

[31]   R. Graveling, A. Sánchez, C. Lewis, S. Groat, M. Van Tongeren, K. Galea, J. Cherrie, Review of occupational hygiene reports on suitability of respiratory protective equipment (RPE), 2009.

[32]   A. Cybulski, J. Moulin, Monoliths in Heterogeneous Catalysis, Catal. Rev. 36 (1994) 179–270. https://doi.org/10.1080/01614949408013925.

[33]   K. Silas, W.A.W.A.K. Ghani, T.S.Y. Choong, U. Rashid, Carbonaceous materials modified catalysts for simultaneous SO2/NOx removal from flue gas: A review, Catal. Rev. Sci. Eng. 61 (2019) 134–161. https://doi.org/10.1080/01614940.2018.1482641.

[34]   M.J.G. Linders, Adsorption processes in gas mask filter canisters: practical aspects, new materials and modeling, in: Recent Adv. Adsorpt. Process. Environ. Prot. Secur., Springer Netherlands, 2007.

[35]   A.J. Blackburn, S.R. Tennisson, A.P. Rawlinson, Filter element, US 2005/0126395 A1, 2005.

[36]   P. Branton, M. Duke, S. Tennison, D.B. Winter, Filter for a smoking article, US9259031 B2, 2016.

[37]   N. Querejeta, M.G. Plaza, F. Rubiera, C. Pevida, T. Avery, S.R. Tennisson, Carbon Monoliths in Adsorption-based Post-combustion CO2 Capture, Energy Procedia. 114 (2017) 2341–2352. https://doi.org/10.1016/j.egypro.2017.03.1366.

[38]   R.P. Ribeiro, T.P. Sauer, F. V. Lopes, R.F. Moreira, C.A. Grande, A.E. Rodrigues, Adsorption of CO2, CH4 and N2 in Activated Carbon Honeycomb monolith, J. Chem. Eng. Data. 53 (2008) 2311–2317. https://doi.org/10.1016/j.gee.2016.09.001.

[39]   B.D. Crittenden, O. Camus, S.P. Perera, T.J. Mays, F. Sanchez-Liarte, S.R. Tennison, E. Crezee, Nonuniform Channels in Adsorbent Monoliths, AIChE J. 57 (2011) 1163–1172. https://doi.org/10.1002/aic.

[40]   B. Crittenden, A. Patton, C. Jouin, S. Perera, S. Tennison, J.A.B. Echevarria, Carbon monoliths: A comparison with granular materials, Adsorption. 11 (2005) 537–541. https://doi.org/10.1007/s10450-005-5981-9.

[41]   H.M. Lee, J. Baek, K.H. An, S.J. Park, Y.K. Park, B.J. Kim, Effects of Pore Structure on n-Butane Adsorption Characteristics of Polymer-Based Activated Carbon, Ind. Eng. Chem. Res. 58 (2019) 736–741. https://doi.org/10.1021/acs.iecr.8b02715.

[42]   Y. Wu, T. Wang, Hydrated salts/expanded graphite composite with high thermal conductivity as a shape-stabilized phase change material for thermal energy storage, Energy Convers. Manag. 101 (2015) 164–171. https://doi.org/10.1016/j.enconman.2015.05.006.

[43]   A.S. Fleischer, Thermal energy storage using phase change materials: Fundamentals and applications, Springer, 2015.

[44]   G. Bartkowiak, A. Marszałek, A. Dąbrowska, Thermal load of mine rescuer in the underwear and protective clothing with phase change materials in simulated utility conditions, Materials (Basel). 13 (2020) 1–16. https://doi.org/10.3390/ma13194320.

[45]   K. Pielichowska, K. Pielichowski, Phase change materials for thermal energy storage, Prog. Mater. Sci. 65 (2014) 67–123. https://doi.org/10.1016/j.pmatsci.2014.03.005.

[46]   Z. Ling, J. Liu, Q. Wang, W. Lin, X. Fang, Z. Zhang, MgCl2·6H2O-Mg(NO3)2·6H2O eutectic/SiO2 composite phase change material with improved thermal reliability and enhanced thermal conductivity, Sol. Energy Mater. Sol. Cells. 172 (2017) 195–201.

https://doi.org/10.1016/j.solmat.2017.07.019.

[47]   X. Huang, G. Alva, L. Liu, G. Fang, Microstructure and thermal properties of cetyl alcohol/high density polyethylene composite phase change materials with carbon fiber as shape-stabilized thermal storage materials, Appl. Energy. 200 (2017) 19–27. https://doi.org/10.1016/j.apenergy.2017.05.074.

[48]   X. Huang, J. Guo, Y. Gong, S. Li, S. Mu, S. Zhang, In-situ preparation of a shape stable phase change material, Renew. Energy. 108 (2017) 244–249. https://doi.org/10.1016/j.renene.2017.02.083.

[49]   A. Sharma, V. V Tyagi, C.R. Chen, D. Buddhi, Review on thermal energy storage with phase change materials and applications, Renew. Sustain. Energy Rev. 13 (2009) 318–345. https://doi.org/10.1016/j.rser.2007.10.005.

[50]   A. Fallahi, G. Guldentops, M. Tao, S. Granados-Focil, S. Van Dessel, Review on solid-solid phase change materials for thermal energy storage: Molecular structure and thermal properties, Appl. Therm. Eng. 127 (2017) 1427–1441. https://doi.org/10.1016/j.applthermaleng.2017.08.161.

[51]   A. Patton, B.D. Crittenden, S.P. Perera, Use of the linear driving force approximation to guide the design of monolithic adsorbents, Trans IChemE, Part A. 82 (2004) 999–1009.

[52]   J. Xiao, L. Tong, C. Deng, P. Bénard, R. Chahine, Simulation of heat and mass transfer in activated carbon tank for hydrogen storage, Int. J. Hydrogen Energy. 35 (2010) 8106–8116. https://doi.org/10.1016/j.ijhydene.2010.01.021.

[53]   M. Saleh Shafeeyan, W. Mohd Ashri Wan Daud, A. Shamiri, A review of mathematical modeling of fixed-bed columns for carbon dioxide adsorption, Chem. Eng. Res. Des. 92 (2014) 961–988. https://doi.org/10.1016/j.cherd.2013.08.018.

[54]   H.K. Versteeg, W. Malalasekera, Conservation laws of fluid motion and boundary conditions, in: An Introd. to Comput. Fluid Dyn. Finite Vol. Method, Longman, London, 1995: pp. 10–40.

[55]   M. Caliano, N. Bianco, G. Graditi, L. Mongibello, Analysis of a phase change material-based unit and of an aluminum foam/phase change material composite-based unit for cold thermal energy storage by numerical simulation, Appl. Energy. 256 (2019) 113921. https://doi.org/10.1016/j.apenergy.2019.113921.

[56]   H. Yang, Y. He, Solving heat transfer problems with phase change via smoothed effective heat capacity and element-free Galerkin methods, Int. Commun. Heat Mass Transf. 37 (2010) 385–392. https://doi.org/10.1016/j.icheatmasstransfer.2009.12.002.

[57]   Z. Liu, Y. Yao, H. Wu, Numerical modeling for solid-liquid phase change phenomena in porous media: Shell-and-tube type latent heat thermal energy storage, Appl. Energy. 112 (2013) 1222–1232. https://doi.org/10.1016/j.apenergy.2013.02.022.

[58]   A. Shahsavar, A.A.A.A. Al-Rashed, S. Entezari, P.T. Sardari, Melting and solidification characteristics of a double-pipe latent heat storage system with sinusoidal wavy channels embedded in a porous medium, Energy. 171 (2019) 751–769. https://doi.org/10.1016/j.energy.2019.01.045.

[59]   D.W. Green, R.H. Perry, Heat and Mass transfer, in: Perry's Chem. Eng. Handb., 8th ed., McGraw-Hill, New York, 2008: pp. 1–83.

[60]   T. Gu, V. Balakotaiah, Impact of heat and mass dispersion and thermal effects on the scale-up of monolith reactors, Chem. Eng. J. 284 (2016) 513–535. https://doi.org/10.1016/j.cej.2015.09.005.

[61]   N. Mladenov, J. Koop, S. Tischer, O. Deutschmann, Modeling of transport and chemistry in channel flows of automotive catalytic converters, Chem. Eng. Sci. 65 (2010) 812–826. https://doi.org/10.1016/j.ces.2009.09.034.

[62]   R.T. Yang, Rate Processes in Adsorbers, in: Gas Sep. by Adsorpt. Process., Elsevier, 1987: pp. 101–139. https://doi.org/10.1016/b978-0-409-90004-0.50007-6.

[63]   P. Brea, J.A. Delgado, V.I. Águeda, M.A. Uguina, Modeling of breakthrough curves of N2, CH4, CO, CO2 and a SMR type off-gas mixture on a fixed bed of BPL activated carbon, Sep. Purif.

Technol. 179 (2017) 61–71. https://doi.org/10.1016/j.seppur.2017.01.054.

[64]   S. Cavenati, C.A. Grande, A.E. Rodrigues, Separation of CH4 / CO2 / N2 mixtures by layered pressure swing adsorption for upgrade of natural gas, Chem. Eng. Sci. 61 (2006) 3893–3906. https://doi.org/10.1016/j.ces.2006.01.023.

[65]   C.A. Grande, A.E. Rodrigues, Propane/propylene separation by Pressure Swing Adsorption using zeolite 4A, Ind. Eng. Chem. Res. 44 (2005) 8815–8829. https://doi.org/10.1021/ie050671b.

[66]   M. Khalighi, S. Farooq, I.A. Karimi, Nonisothermal pore diffusion model for a kinetically controlled pressure swing adsorption process, Ind. Eng. Chem. Res. 51 (2012) 10659–10670. https://doi.org/10.1021/ie3004539.

[67]   E. Glueckauf, J.I. Coates, Theory of Chromatogruphy. Part IV. The Influence of Incomplete Equilibrium on the Front Boundary of Chrromatograms and on the Effectiveness of Separation, J. Chem. Soc. 241 (1947) 1315–1321.

[68]   S. Farooq, D.M. Ruthven, Heat Effects in Adsorption Column Dynamics. 2. Experimental Validation of the One-Dimensional Model, Ind. Eng. Chem. Res. 29 (1990) 1084–1090. https://doi.org/10.1021/ie00102a020.

[69]   F. Birkmann, C. Pasel, M. Luckas, D. Bathen, Trace Adsorption of Ethane, Propane, and n-Butane on Microporous Activated Carbon and Zeolite 13X at Low Temperatures, J. Chem. Eng. Data. 62 (2017) 1973–1982. https://doi.org/10.1021/acs.jced.6b01068.

[70]   J.M. Coulson, J.F. Richardson, Flow of liquids in pipes and open channels, in: Chem. Eng. Fluid Flow, Heat Transf. Mass Transf., Sixth, Butterworth-Heinemann, Oxford, 1999.

[71]   T. Valdés-Solís, M.J.G. Linders, F. Kapteijn, G. Marbán, A.B. Fuertes, Adsorption and breakthrough performance of carbon-coated ceramic monoliths at low concentration of n-butane, Chem. Eng. Sci. 59 (2004) 2791–2800. https://doi.org/10.1016/j.ces.2004.03.025.